Imaging the structural style of an active normal fault through multi-disciplinary geophysical investigation: a case study from the Mw 6.1, 2009 L'Aquila earthquake region (central Italy).

Fabio Villani[1]*, Stefano Pucci[2], Riccardo Civico[2], Paolo Marco De Martini[2], Iacopo Nicolosi[2], Francesca D'Ajello Caracciolo[2], Roberto Carluccio[2], Giuseppe Di Giulio[1], Maurizio Vassallo[1], Alessandra Smedile[1], Daniela Pantosti[2]

1: Istituto Nazionale di Geofisica e Vulcanologia, via dell'Arcivescovado 8 – 67100 L'Aquila, Italy

2: Istituto Nazionale di Geofisica e Vulcanologia, via di Vigna Murata 605 - 00143 Rome, Italy

*: Corresponding author: fabio.villani@ingv.it

SUMMARY

The normal fault-system responsible of the 2009 Mw 6.1 L'Aquila earthquake (Paganica-San Demetrio fault-system) comprises several narrow, fault-parallel valleys of controversial origin. We investigated a key section of the south-eastern portion of this fault network along the small Verupola Valley. In order to characterize its nature and possible tectonic activity, we applied multiple-geosciences techniques able to image at depth the structure associated to this peculiar landform. We integrated magnetometry, 2-D P-wave and resistivity tomography, surface waves and seismic noise analysis coupled with field mapping, shallow boreholes and trenching.

According to our results, the Verupola Valley is a ~30-40 m-deep graben controlled by a SW-dipping master fault and synthetic splays paired with an antithetic NE-dipping fault. The SW-dipping splays are active and cut very shallow (<2 m deep) Late Pleistocene sediments. The small amount of cumulated vertical offset (~15 m) across the conjugated system may indicate a young fault inception or very low Quaternary slip-rates.

Due to its structural continuity with the adjacent mapped strands of the Paganica – San Demetrio fault network, we relate the Verupola Valley to the recent activity of the south-eastern segment of this fault

system. We also suggest that other fault-parallel valleys can have the same tectonic origin and setting of the Verupola Valley. This latter represents a scale-independent analogue from metric scale (exposed in the paleoseismological trenches) to the Middle Aterno Basin scale (seen from seismic profiles and fault mapping). Overall, the imaged structural style is coherent with the regional tectonic setting due to Quaternary crustal extension.

Keywords:

51. Magnetic and electrical properties

110. Seismicity and tectonics

118. Site effects

119. Seismic tomography

140. Continental neotectonics

166. Fractures and faults

1 INTRODUCTION

The recognition and characterization of active faults in terms of geometry, type of movement, and rates of activity, is critical for the evaluation of the seismic potential of a region but also for the correct planning of the land use (*e.g.* surface faulting hazard). These studies are based on tectonic geomorphology and Quaternary geology investigations, however shallow subsurface geophysical imaging of fault zones has become a successful practice (among the others: Demanet *et al.* 2001; Shuhab *et al.* 2013). Seismic and electrical methods are the most commonly employed (Griffiths & Barker, 1993; Storz *et al.* 2000; Sheley *et al.* 2003; Dorn *et al.* 2010; Bruno *et al.* 2013) since they provide a good compromise between a high spatial

47 resolution and a significant subsurface investigation depth (from some tenths up to hundreds of meters).
48 Magnetic surveys are also used for locating buried faults and structures (Blakely *et al.*, 1995; Gibson *et al.*
49 1996; Speranza *et al.* 2009). However, in some cases the geological conditions may lead to ambiguities in
50 the interpretation of these geophysical datasets. For example, seismic velocity and electrical resistivity may
51 display a positive correlation (Meju *et al.* 2003), but sometimes their spatial variations are quite discrepant.
52 To overcome possible pitfalls, their combination and a cross-consistency check is recommended in the
53 geological interpretation.

54 The combined use of different near surface geophysical surveys is a powerful tool in active tectonic studies,
55 as well as in paleoseismology (Meghraoui *et al.* 2000; Wise *et al.* 2003; Ahmad *et al.* 2009; Improta *et al.*
56 2010; Galli *et al.* 2013), providing a larger exploration depth with respect to paleoseismic trenches and
57 boreholes (Mc Calpin 2009). Calibration of observed data through boreholes and/or
58 geognostic/paleoseismic trenches is highly effective in the imaging process. Such integrated investigations
59 are profitable where geological factors (lithological heterogeneity, structural complexity, low deformations
60 rates) coupled with exogenous factors (wet climate and high sedimentation/erosion rate, urbanization and
61 anthropic modification) may hamper the explicit surface expression of active fault systems and the
62 development of unambiguous tectonics landforms. We present a case-study from the central Apennines of
63 Italy, a region of active extension, intense seismicity and complex surface geology struck by the 6th April
64 2009 Mw 6.1 L'Aquila earthquake (Fig. 1). The selected area (Fig. 2) focuses on a portion of the Paganica –
65 San Demetrio normal fault-system (hereinafter PSDFS) activated during the seismic sequence.

66 While the Paganica sector has been extensively studied in terms of surface geology, paleoseismology and
67 shallow geophysics (among the others: MS–AQ Working Group 2010; Giaccio *et al.* 2012; Improta *et al.*
68 2012), the SE part is less explored. Our focus is the subsurface imaging of one (the Verupola Valley) among
69 many narrow, dry and fault-parallel valleys that occur just along the San Demetrio sector. Due to the lack of
70 fault outcrops and the long-standing agricultural practices, the tectonic origin of the investigated valley is
71 uncertain, as other morphogenetic factors are also likely (*i.e.*, fluvial erosion, karst processes). Unveiling the
72 origin of this small (<1 km^2) basin may help understanding the tectonic evolution of the whole area struck

by the 2009 earthquake (>200 km^2) and, more generally, the large-scale evolutionary trend of the central Apennines extension. In fact, this valley represents an analogue of other unexplored small continental basins parallel to the Quaternary fault network (Fig. 1a): their tectonic or non-tectonic origin is critical to evaluate the correct length and throw of each fault strand, as well as the geometric relationships between adjacent segments (a fundamental factor controlling fault interaction; Gupta & Scholz, 2000).

To this aim we integrated different geophysical techniques with shallow boreholes and geognostic trenches. This work shows the great potential of integrated investigations to support morphotectonic studies aimed at the identification and characterization of active faults/structures.

This paper consists of: a description of the geological setting of the study area (Section 2); a short methodological outline (Section 3); a description of the collected data (Section 4); a discussion of their interpretation along with their possible geological implications (Section 5).

2 GEOLOGICAL SETTING AND QUATERNARY TECTONIC FRAMEWORK

2.1 The Middle Aterno Valley

The study area is located in the Middle Aterno Valley, in the inner sector of the central Apennines (Figs 1 and 2). This is a NE-verging Neogene fold-and-thrust belt mainly made of Mesozoic-Tertiary carbonates and siliciclastics (Centamore *et al.* 2006; Patacca *et al.* 2008). Pliocene-Quaternary extension affected the chain axis generating normal fault-systems consisting of 5- to 15 km-long, NW- to WNW-trending and generally SW-dipping segments (Ghisetti & Vezzani 1999; Galadini & Galli 2000; Fig. 1b). Many intramontane basins developed in their hangingwall (*e.g.* Bosi *et al.* 2003). The Middle Aterno Valley encloses several fluvio-lacustrine depressions to the SE of L'Aquila, related to the PSDFS long-term activity (Pucci *et al.* 2014 and references therein).

In this region current NE-extension (Montone *et al.* 2012 and references therein) with ~3 mm/yr horizontal deformation rates (Carafa & Barba 2011; Devoti *et al.* 2011) is responsible for widespread upper crustal

97 seismicity, and several strong and damaging (M>6) earthquakes occurred in the last centuries (Chiarabba *et*
98 *al.* 2005; Rovida *et al*. 2011). The 6th April 2009, Mw 6.1 earthquake was generated by a ~13-17-km long
99 normal fault belonging to the NW sector of the PSDFS (Atzori *et al*. 2009; Chiarabba *et al.* 2009), showing
100 evidence of coseismic surface faulting (Falcucci *et al.* 2009; Boncio *et al.* 2010; Emergeo Working Group
101 2010; Galli *et al.* 2010; Vittori *et al.* 2011). Paleoseismological trenching along this coseismic free-face
102 revealed ~50° SW-dipping principal slip surfaces displacing late Pleistocene – Holocene sediments, during at
103 least 4 pre-2009 large earthquakes in the last ~3 kyr (Cinti *et al.* 2011; see also Fig. 10d). Detailed analyses
104 of the 2009 seismic sequence and aftershock relocations provided sights into the upper crustal active
105 normal fault architecture of this sector of the Apennines, characterized by a conjugate system of en-
106 échelon, <60° SW-dipping, NW-trending master faults (down to 10-12 km depth) and high-angle antithetic
107 faults (Chiaraluce *et al.* 2011; Valoroso *et al.* 2013, 2014; Fig. 1c).

108 According to several authors, the 6th April 2009 earthquake normal fault belongs to the PSDFS (Fig. 1a). The
109 PSDFS comprises two main sectors: 1) the Paganica sector to the NW, characterized by a narrow
110 deformation zone and a relatively small hangingwall Quaternary basin affected by few fault splays; 2) the
111 San Demetrio sector to the SE, with a set of parallel, km-spaced fault splays that exhume and dissect a
112 wider Quaternary basin. A peculiar morphological feature of the PSDFS is the presence of <1 km large, dry,
113 fault-system-parallel valleys (Fig. 1a). Their trends, mostly orthogonal to the SW-dip of the northern slope of
114 the Middle Aterno basin, and the Holocene infill suggest a persistent tectonic activity of the PSDSF. These
115 dry valleys are mostly carved onto Quaternary fluvio-lacustrine gravels, conglomerates and sandy-silty
116 deposits (Pucci *et al.* 2014). Although there is sometimes clear geomorphic evidence, the erodible
117 continental sediments and the debris cover along the foothills often hinder fault plane outcrops. Moreover,
118 complex partitioning of brittle deformation in such sediments originates faint fault scarps and diffuse
119 fracture patterns, making the reconstruction of the local structural setting difficult.
120

121 **2.2 The survey site**

The survey site is the ~1.5 km-long, NW-trending Verupola Valley (Figs 1a and 2). The valley is parallel to the NW termination of the San Giovanni fault (SGF, thereinafter; Fig. 1b), a segment of the PSDFS giving rise to a ~5 km-long scarp (Giaccio *et al.* 2012; Civico *et al.* submitted; Pucci *et al.* 2014).

In this site marine Cretaceous and Miocene limestones are covered by continental deposits consisting of four depositional cycles (Fig. 2; Bosi & Bertini 1970; Bertini & Bosi 1993), from bottom to top: 1) lacustrine and fluvio-lacustrine sequence (*Limi di San Nicandro Fm*.), composed of whitish silts and clayey silts with gravel lenses, up to 100 m-thick; 2) alluvial sequence (*Vall'Orsa Fm*.) partially heteropic with the *Limi di San Nicandro*, consisting of deltaic carbonatic conglomerates showing foreset and bottomset beds; 3) alluvial fan sequence (*Valle Inferno Fm*.), consisting of well bedded carbonatic conglomerates showing topset beds, with sparse silty layers and paleosoils; 4) upper fluvial and alluvial sequence, made of sands and gravels or silts, interbedded with volcanoclastic layers (*San Mauro Fm*.). Thanks to biostratigraphical analyses, the *Limi di San Nicandro* and *Vall'Orsa Fms*. are dated Early Pleistocene, whereas, by means of tephrochronological and paleomagnetic analyses (Giaccio *et al.* 2012; Mancini *et al.* 2012) the *San Mauro Fm*. is dated to the Middle-Late Pleistocene.

The Verupola Valley (Fig. 2) is carved mainly in the *Vall'Orsa Fm*., it hosts recent colluvial deposits of unknown thickness and presents also some small tributary seasonal valleys running from the NE flank. The *Vall'Orsa Fm*. foreset beds strike differently, dipping ~N135° and ~N170° north and south of the valley respectively (Figs 2 and S1). South of the Verupola Valley, the *Vall'Orsa Fm*. has a smaller thickness (<20 m; data from quarry in Fig. 2) and presents a flat, erosional top surface. Conversely, to the north the *Vall'Orsa Fm*. is thicker and presents a morphologic SW-dipping scarp (>50 m high), coupled with a smaller (~3 m high) discontinuous scarplet running at its base. SE of the survey site, the geological post-Early Pleistocene vertical offset across the SGF is ~100 m (Pucci *et al.* 2014).

Despite the evident morphologic scarp along the NE side of the Verupola Valley suggests a northern prolongation of the SGF, no clear structural elements crop out supporting its tectonic genesis. All this makes the Verupola Valley a favourable site to image its subsurface structure, as well as a good analogue for the other NW-trending valleys in the area.

3 METHODS

In order to provide a large-scale picture of the basin subsurface we performed 1 magnetic survey that covers a 0.25 km^2 area and 2 NE-trending electrical resistivity tomography (ERT) profiles from side to side . Moreover, we acquired 1 high-resolution seismic profile and 2 additional shorter ERT profiles to explore the shallow subsurface of the ~3 m high morphologic scarp. We also made 8 seismic noise recordings close to the seismic line. Location of geophysical surveys is shown in Fig. 2, and some details of the surveys are indicated in Table 1. The geophysical surveys are corroborated by available detailed field data (Pucci *et al.* 2014), moreover we performed a new structural survey of *Vall'Orsa Fm.* fractures pattern and 6 shallow boreholes (location in Fig. 5d) that were drilled with a vibracoring (gasoline percussion hammer). We then optimized the location of 1 geognostic trench based on geophysical data and boreholes that at its turn was used to test the correctness of the geophysical interpretation.

The integration of all these sets of data is uncommon in the study of active fault/structures in Italy, as in general only a couple of them are considered (see, among the others: Salvi *et al.* 2003; Improta *et al.* 2010; Roberts *et al.* 2010; Giocoli *et al.* 2011; Galli *et al.* 2013).

In the following we briefly describe the different applied approaches.

3.1 Magnetometry

We used a scalar magnetometer as rover unit (GemSystem GSM 19 Overhauser) and a proton precession magnetometer as base station (GemSystem GSM19) for monitoring magnetic field diurnal variations. After clock synchronization between the two magnetometers, we contemporaneously acquired base station and rover unit magnetic values to remove the magnetic field diurnal variations from rover measures (Time Reduction correction), and georeferenced the magnetic stations by the rover internal GPS board. We acquired 15 parallel magnetic profiles spaced ~50 m apart along N30° direction (~5 km total length and

~2000 stations) following the *walking mode* procedure: (1) the magnetometer unit acquires at 1 Hz sampling frequency; (2) the operator is walking along profiles (~1 measure / 2 m) maintaining the rover unit sensor ~2 m high to minimize ground noise; (3) the base station sensor is kept at a height of ~3 m with a sampling rate of 1 measure every 30 seconds. We obtained the anomaly values by subtracting the calculated main field component of the Earth's Magnetic Field from each diurnally corrected survey point using the 11^{th} generation of the International Geomagnetic Reference Field model. We interpolated measured data using a 5 m grid. We also collected some superficial susceptibility measures over continental sediments of the Verupola Valley, showing a mean value of $5*10^{-3}$ SI. These measures are not representative of the overall sediments but could provide a reference value of their magnetic properties.

3.2 Electrical resistivity tomography (ERT)

We acquired 4 electrical resistivity profiles (Fig. 2 and Table 1) with different configurations of quadrupoles (Table 1), looking for a good compromise between vertical and horizontal resolution (Loke & Barker 1995). We injected a square wave signal for 250 ms observing relatively homogeneous ρ check values between adjacent electrodes (0.5-1.5 KΩ*m). The field data (pseudo-section method, *sensu* Hallof, 1957) were input to a 2-D smoothness-constrained least squares inversion algorithm, where the investigated area is subdivided into rectangular blocks, half the electrode spacing wide (Constable *et al.* 1987; Loke & Dahlin 2002).

3.3 Seismic tomography

We used a 72 vertical geophones array and a sledgehammer (Fig. 2; Table 1). To obtain a robust 2-D Vp tomographic model, we accurately hand-picked 5254 first arrival traveltimes (rms picking error ~1.2 ms; Fig. S2). The traveltimes were input to a non-linear tomographic code following a multi-scale optimization scheme based on a mixed global-random and local search (Herrero *et al.* 2000; Improta *et al.* 2002). *Vp* models are parameterized through a grid of nodes, and traveltimes are computed with the finite-difference

197 solution of the eikonal equation (Podvin & Lecomte, 1991). The multi-scale approach allows stable
198 convergence of the inversion process with a gradual increase in the number of model parameters during
199 consecutive inversion runs. The early parameterization levels retrieve the long-wavelength features of the
200 medium, while models with a higher number of nodes recover the shorter ones. We compared the final rms
201 traveltime residuals with the average picking error (Fig. S2), and assessed model resolution by *a-posteriori*
202 checkerboard tests (Fig. S3). We show two representative *Vp* models: 1) a long-wavelength model that
203 depicts the large-scale structure of the basin NE border (Section 4.1); 2) a short-wavelength model that
204 details only the shallower portion (Section 4.2).

205

206 **3.4 Surface waves and noise analysis**

207 We processed seismic traces previously described by the conventional frequency-wavenumber (F-K)
208 analysis for deriving dispersion curves of Rayleigh waves (Tokimatsu 1997; Kvaerna & Ringdahl 1986;
209 Ohrnberger *et al.* 2004). The dispersion curves are generally associated to the fundamental mode of
210 Rayleigh waves, providing information on shear-wave velocity (*Vs*) and on layers thickness of the retrieved
211 velocity model (Xia et al. 1999; Socco & Strobbia 2004).

212 Further, we recorded ambient noise data using 24-bit digitizers (Reftek130) and three-components
213 velocimeters (Le3d with eigenfrequency of 0.2 Hz) to get H/V curves (Nakamura 1989), which are computed
214 as the ratio of the Fourier amplitude spectra between the horizontal and the vertical components. We
215 made 4 noise measurements recordings along the seismic line (VER1, VER2, VER3 and VER4; few hours of
216 the 21th of February 2013) and other 4 measurements (VER10, VER11, VER12 and VER13; during an entire
217 night, between the 11th and the 12th of July 2013) inside an adjacent paleoseismological trench (not
218 discussed in this paper). H/V curves provide the soil resonance (f0) associated to the peak frequency, which
219 for 1-D structures is closely linked to the mean properties (thickness and *Vs*) of the soft soil (Fäh *et al.* 2001*;*
220 Bonnefoy-Claudet *et al.* 2006*)*. Directional H/V ratios (computed rotating the seismic signal along the
221 horizontal plane using regular bins; Spudich *et al.* 1996), can indicate (if any) the direction of the maximum

polarization of the ground motion. Some authors (Burjánek *et al.* 2010; Pischiutta *et al.* 2012) evidenced a connection between the strike of maximum polarization and the azimuthal distribution of fractures. The dispersion curves, the resonance frequency, and the polarization directions are used to infer information on the *Vs* of the infilling material, on the seismic basement depth, and on the possible influence of fracture patterns on polarization direction (Section 4.3).

4 Data and Results

4.1 Large-scale basin imaging (magnetic, ERT and *Vp* data)

Fig. 3 shows the gridded magnetic anomalies measured in the field after the application of the reduction to magnetic pole operator (panel a) and the modulus of their horizontal components (panel b).

The most noticeable feature is a 70-100 m wide, NW-trending anomaly along the valley (Fig. 3a). It delineates the Verupola basin axis where magnetized continental sediments (>70 nT) reach their maximum thickness. On the other hand, the conglomerate and carbonate domains show no magnetic signature. Fig. 3b shows NW-trending horizontal modulus maxima (>90-100 nT) that may represent the surface projection of the deep magnetic sources edges, taking in consideration that non-vertical contacts produce anomalies that are not exactly located over the source boundaries (Blakely & Simpson 1986). In this case, these maxima indicate discontinuities separating the susceptive continental infill of the Verupola Valley from the poorly susceptive conglomerate-carbonate host rocks.

The anomalies in Fig. 3a show a change in direction and intensity in the central part of the basin, varying from N150° and <50 nT to N120° and >100 nT in the NW and the SE sectors, respectively. From a magnetic point of view, this indicates a change in strike and thickening of susceptive basin infill towards the SE (Section 5).

Fig. 4a shows a representative long-wavelength *Vp* model (checkerboard test and plot of rays density in Fig. S3a). The lower portion displays a high-*Vp* region (*Vp*>2750-3000 m/s) deepening to the SW. The top of the

high-*Vp* region is a main refracting interface, as evidenced by the vertical velocity gradient (at x=10-70 m) and the rays pattern (Fig. S3a). Above the high-*Vp* body, a widening of the Vp~2000-2250 m/s region is evident at x=30-90 m. Similarly, the top of this region is an important refracting interface (Fig. S3a) laying at ~10-15 m depth. In the upper part, a shallow, thin (~5 m), low-*Vp* (<1000 m/s) layer thickens to the SW. The deflection of iso-velocity contour lines marks lateral *Vp* contrasts at x=15-20 m and, to a lesser extent, at x=80-90 m (F2 and F1 respectively, Fig. 4a).

The main features of models ERT3 (Fig. 4c) and ERT4 (Fig. 4e) are: 1) a low-resistivity (ρ<80 Ohm*m) region extending for ~60-100 m in the middle portion and deepening ~30-40 m below the ground surface; 2) high-resistivity bodies (ρ>500 Ohm*m) on both the SW and NE sides. Lateral resistivity changes suggest a SW-dipping discontinuity (F2) at x=130-140 m and at x=180-200 m (although less clear) on the NE side of ERT3 and ERT4, respectively. Along the SW side of the models, a NE-dipping discontinuity (F3) is visible at x=80-90 m and x=120-140 m on ERT3 and ERT4, respectively. Moreover, the bumpy geometry of the top of the high-resistivity body (ρ>500 Ohm*m) in the NE portions of the models, suggests an additional SW-dipping discontinuity (F1) at x=170-180 m and x=250-280 m along ERT3 and ERT4, respectively. 2-D cross sections from the magnetic anomalies and the horizontal components maps (Figs 3a and 3b) are compared with the long-wavelength *Vp* model (Fig. 4b), and both the ERT3 and ERT4 models (Figs 4d and 4f). From comparison with ERT results we note that: 1) the thickest and widest regions of low ρ match the zones with the highest magnetic intensities (thin black curve), pointing out a remarkable positive correlation (Fig. 10b; Section 5.2); 2) the modulus of horizontal components (thick red curve) shows maxima located at the basin edges. These maxima correspond to sharp lateral resistivity contrasts on ERT3, whereas one clear maximum is coinciding with that at x=110 m over ERT4 and two smaller maxima at x=160 and x=250 m are evident. These lateral resistivity changes depict dipping interfaces rather than vertical discontinuities, so this may explain why the peak of horizontal component modulus is slightly shifted towards their down-dipping side.

4.2 Shallow basin imaging (ERT and *Vp* data)

We also investigated the shallow subsurface of the ~3 m high scarplet running at the NE basin border. Figs 5a, 5c and 5d show respectively ERT1, ERT2 models and a representative short-wavelength *Vp* model (checkerboard test and plot of rays density in Fig. S3b).

ERT1 model (Fig. 5a) shows an abrupt lateral resistivity change at x=50-55 m (F1). To the SW a ~10 m thick low-resistivity (ρ<20 Ohm*m) lens is visible above a possible additional discontinuity at x=30 m (F2). The ERT2 model (Fig. 5c) shows a shallow high-resistivity body (ρ>500 Ohm*m at ~2 m depth) in the NE portion, which gradually deepens towards the SW under a low-resistivity layer (ρ~10-40 Ohm*m). The low-resistivity region (ρ<80 Ohm*m) is >20 m thick in this part of the model. The iso-resistivity contours show a lateral increase of ρ moving to the NE at x=35-50 m (F2). The bumpy geometry of the top of the high-resistivity body at x=75-80 m, suggests another SW-dipping discontinuity (F1) just below the main scarp.

The short-wavelength *Vp* model (Fig. 5d) explores a shallower (~10 m depth) region. Checkerboard test (Fig. S3b) indicates a resolution depth of ~8-10 m. The very shallow layers (<4 m deep) with *Vp* <400 m/s thicken to the SW. Ray-density plot (Fig. S3b) suggests a main SW-dipping refracting interface at ~7-8 m depth, close to the lower limit of the resolved region, where *Vp* increases from 1500 to 2000 m/s. A bump of the 1500 m/s contour depicts an evident rise of the high-*Vp* body below the main scarp, which may be related to a discontinuity at x=85 m (F1).

Comparing the ERT1, ERT2 and *Vp* models to the magnetic data (Figs 4b and 5b), the regions of both low-ρ/low-*Vp* match the locations of high positive magnetic anomaly.

4.3 Additional geophysical constraints on the basin shallow structure (dispersion and H/V curves)

We derived dispersion curves considering two geophones groups independently within the linear seismic line (#1-36 and #37-72, to the SW and to the NE of the scarp, respectively), using traces from the central common shot gather (CSG) as shown in Fig. 6a. Seismic traces show larger duration and development of surface waves only in the left part (group of geophones #1-36), indicating low-velocity sediments SW of the

scarp, consistently with tomographic results (Figs 4a and 5d). For geophones #1-36 a clear dispersion curve is obtained in the 20-60 Hz range (Fig. 6b), with apparent phase velocities ranging from ~320 m/s to ~180 m/s, respectively. In the NE part of the array (corresponding to geophones #37-72), the dispersion curve is clearly limited at ~35 Hz (Fig. 6c). The equivalent wavelengths are λ~17 m at 20 Hz and λ~3 m at 60 Hz, resulting in a maximum investigation depth of ~5 m (~λ/3).

Using traces at different offsets with a limited number of geophones, F-K analysis shows again significant variations of phase velocities (Fig. 6d). The dispersion curves SW of the scarp (coloured curves in Fig. 6d) indicate lower *Vs* and lower frequency of investigation with respect to the remaining portion of the array (black curves in Fig. 6d). These results confirm a sharp change of surface waves behaviour across the scarp, corroborating the presence of a discontinuity at x=80-90 m (F1) at depth.

H/V curves for stations VER1, VER2, VER3 and VER4 in Fig. 7a (location in Fig. 4a) show f0~1.3-1.4 Hz. Other narrow peaks are visible in the 10-30 Hz high-frequency band (Fig. 7b). H/V curves from stations inside the paleoseismic trench (Fig. 7b) have no high-frequency peaks, whereas at low-frequency H/V curves show a bump in the range 1.3-2.7 Hz, which is independent from the receivers position (Fig. 7b). The comparison between noise measurements inside and outside the trench suggests that anthropic activities, or the ~3 m thick layer removed to dig the trench, were likely responsible for the >10 Hz peaks observed in the surface measurements. Whereas the cause of the low-frequency bump at 1.3-2.7 Hz (Fig. 7b) is not clear, the directional H/V patterns (Fig. 7c) suggest two peaks close in frequency. Anyway, by applying the 1-D formula *f0=Vs/4H* (assuming f0~1.3 Hz and *Vs*~200 m/s for the basin infill sediments), we get a ~35-40 m deep seismic basement below stations far from the scarp, in agreement with the results from *Vp* (Fig. 4a) and ERT3 (Fig. 4c) models.

The wavefield of ambient noise is polarized around f0 in the N50°-80° direction (Fig. 7c). The N50° direction is about orthogonal to the general strike of the inferred fault F1 (Section 5). Similar results were previously observed in other fault zones in Italy and California (Di Giulio *et al.* 2009; Pischiutta *et al.* 2012). The structural data on extensional joints affecting the *Vall'Orsa Fm.* conglomerates in the footwall of the SGF

320 (Fig. S1) suggest that the N50°-80° polarization direction is also almost orthogonal to the main joint
321 direction (N158°).

322 During the noise recordings, we detected at VER2, VER3 and VER4 (VER1 was temporarily powered off) a
323 weak local earthquake (M_L 1.7, February 21th 2013, 15:20:11 UTC) located 25 km north of the study area
324 (http://www.iside.rm.ingv.it). Although the stations are very close each other (maximum relative distance is
325 148 m), the recorded seismograms show clear evidence of site-effects (Fig. 8a). As expected, the smallest
326 and largest amplitudes are recorded by the stations to the NE of the scarp (VER2) and within the Verupola
327 Valley (VER4), respectively. Accordingly, the spectral amplitudes for both the horizontal and vertical
328 components of VER4 are larger than those of VER2 within 3-15 Hz (Figs 8b, 8c, 8d). This agrees with the
329 thickening of low velocity sediments in the hangingwall of F1, as revealed by seismic tomography (Figs 4a
330 and 5d) and surface-waves dispersion (Fig. 6), indicating a typical amplification effect related to a basin filled
331 with low-velocity sediments.

332

333 **4.4 Boreholes and trench data**

334 In Fig. S4 we report the detailed stratigraphy of all cores but C3 (because only 1.65 m deep, as
335 conglomerates were very shallow). The upper part of the cores (between 1.8 m and 6 m depth) is
336 characterized by a monotonous succession of red to brown sandy and silty clayey soils with sparse gravels
337 and some white calcrete levels. The boreholes reached at ~2-5 m depth a weathered conglomerate showing
338 at places a silty matrix and calcareous concretions at the top.

339 In order to directly investigate the discontinuity F1 in its shallowest position (along ERT1 at x~50 m), we
340 excavated a small trench (Fig. 2), ~2.5 m deep and ~30 m long between ERT1 and ERT2 profiles. A simplified
341 log is reported in Fig. 9 (the projected trench outline is shown on ERT1, Fig. 5a). The walls expose a
342 succession of SW-dipping brown to reddish sandy and silty soils in the SW part, with abundant gravels
343 intercalations to the NE. A clear and very shallow (<1 m) fault zone dipping 50° to the SW with normal
344 kinematics is visible at x=24 m. The hangingwall hosts brownish alluvial sands, gravels, and silty soils with a

caliche horizon (possibly Late Pleistocene; Cinti *et al.* 2011), whereas the footwall hosts the *Vall'Orsa Fm.* conglomerates and whitish calcareous concretions. Unfortunately, the upper part of the excavation is affected by anthropic modification that removed late Holocene deposition useful to testify the most recent fault activity.

5. Discussion

5.1 Calibration of geophysical data

By comparing the stratigraphy of the boreholes (Fig. S4) and that exposed in the geognostic trench (Fig. 9) with the short-wavelength *Vp* model (Fig. 5d) and ERT2 profile (Fig. 5c), we can attribute very low *Vp* (<600 m/s) and ρ (<40 Ohm*m) values to silty sands and clays (see also vertical *Vp* and *ρ* profiles compared with boreholes stratigraphy in Fig. S4). The dispersion curves indicate, for silty sands and clay, *Vs* ~200-250 m/s (Fig. 6). The basal conglomerates found in the boreholes correspond to an increase in *Vp* (>800-1000 m/s) and ρ (>90 Ohm*m). Higher *Vp* (~1600-1800 m/s) and ρ (>500 Ohm*m) regions are >5 m deep. We interpret the bottom layer of the boreholes as the weathered top of the Early Pleistocene *Vall'Orsa Fm*., widely exposed in the footwall of the SGF, whereas the *Vall'Orsa* conglomerates should be located at least 2 m deeper, in coincidence of the main refracting interface ~6-8 m deep with *Vp*~1500-2000 m/s in the short-wavelength *Vp* model (Fig. S3b).

As regards deeper rocks, some hints on their nature are provided by the *Vp* long-wavelength model (Fig. 4a): the ray density plot (Fig. S3a) suggests that the top of the 3000 m/s region represents a ~20-25 m deep refracting interface, possibly the contact between conglomerates and marine carbonates. In fact, according to tomographic images calibrated by shallow boreholes in the nearby Paganica basin (Improta *et al.* 2012), *Vp*>3250 m/s may indicate a highly fractured, shallow carbonate bedrock.

Overall, ρ and *Vp* values show a positive correlation (Fig. S5) to reconstruct stratigraphy in the shallow subsurface.

5.2 Basin geometry and structure

We interpret the Verupola Valley as a graben (Fig. 10a). It is bounded by two almost parallel SW-dipping normal faults on the NE side (F1 and F2, which are part of the SGF) and on the SW side by a NE-dipping antithetic fault (F3). Downthrown and uplifted blocks have contrasting physical properties (namely ρ, *Vp*, *Vs*, magnetization).

The semi-quantitative subsurface structural scheme in Fig. 10a is based on the integration of all collected data. We use a linear relation between depth of conductive layer (ρ<80 Ohm*m, from the four ERT models; Fig. 10b) and associated positive magnetic anomaly, to obtain the conductive infill isopachs. Although 2nd order polynomial interpolation provided a slight better correlation coefficient, the average topography of the two resulting isopach maps differs by less than ~10% (Fig. S6). The linear relation approximation we use is then acceptable, since even taking into account the non-linear magnetic component effect, the uncertainty on the basin depth is comparable with ERT spatial resolution (data were acquired with 2 m and 5 m electrodes spacing; Table 1).

In the basin reconstruction, we see small depocenters (>30 m deep) controlled by displacement gradient along the bounding faults. We also recognize a thickening of infill deposits containing a significant fraction of magnetic minerals to the SE; this can be attributed to the reworking of the susceptive *San Mauro Fm*. (Section 2.2). Moreover, a slight change in the strike of faults is recognizable, being N150° in the NW and N120° in the SE. Such a change in orientation seems to mimic also changes in modal strike class of extensional joints affecting the outcropping conglomerates of *Vall'Orsa Fm.* (Fig. S1).

5.3 Faults location, geometry and depth

ERT1 model shows an excellent match between the inferred fault (F1) and the true fault zone recovered in the trench (Figs 5a and 9). Note that the integrated geophysical approach highlights the presence of a larger

number of faults controlling the Verupola Valley with respect to those inferred by the sole morphotectonic approach (Fig. 2). Uncertainty in fault location is on the order of ~10 m or even less (Sections 4.1 and 4.2).

As regards fault geometry, ERT and *Vp* models depict dipping interfaces and the slight shift of corresponding magnetic anomalies towards the down-dipping side of the ρ and *Vp* discontinuities; this rules out near-vertical contacts. Furthermore, the 50° dipping fault zone in the trench suggests that the other imaged faults have a similar dip with the exception of the NE-dipping fault, for that dips ~70°.

The data show that the SW-dipping F1 and F2 faults have a very shallow upper tip and displace very shallow sediments, indicating post- Late Pleistocene activity. In particular, ERT1, ERT2 and the short-wavelength *Vp* models indicate that fault F1 upper tip is <2 m deep, and this is confirmed by trench data. In Fig. 5d we interpret the evident ~2m deflection of 1000-1500 m/s contours and a comparable thickening of the Vp<500 m/s region below the scarp (x=85 m), as the tomographic image of the most recent cumulated offset (<2 m) along F1. Note that the scarp is entirely made of sandy-clay deposits (core C4, Fig. S4), thus supporting its recent age. The shallow SW-dipping fault zone, together with the dominant pattern of extensional joints affecting *Vall'Orsa Fm.,* could be also related to the polarized strikes resulting from the directional H/V curves (Fig. 7c). While the SW-dipping faults are very shallow, the F3 upper termination seems to be confined at ~10-15 m depth.

5.4 Structural style and geological implications

Our geological interpretation is condensed in a representative cross-section (Fig. 10c). This is done 1) considering the thickness of the Early Pleistocene conglomerates nearly constant (<20 m) according to outcrop evidence and the *Vp* model (Section 2.2; Figs 2 and 4a), and 2) hypothesizing the antithetic fault may intercept the SW-dipping master fault at quite shallow depth (~100 m).

A noticeable feature is the asymmetry of the basin infill due to the thickening of syn-tectonic sediments close to the antithetic fault that denotes a depocenter far from the master fault. This setting is a response

417 of the enhanced hangingwall collapse guided by the higher dip along the antithetic fault F3 with respect to
418 the 50° of the master fault F1, but also because of the several synthetic faults. Thick clayey deposits close to
419 fault F3 (Figs 4c and 4e) indicate that the long-term asymmetric subsidence in this portion of the basin
420 favoured entrapment of fine sediments.

421 The overall cumulated post-Early Pleistocene vertical offset of the conjugated normal fault-system across
422 the Verupola valley is only ~15 m, whereas the hangingwall collapse given by the total vertical slip of
423 competing antithetic and synthetic splays is ~35-40 m inside the basin. Therefore, a major consequence of
424 this structural style is that even low amounts of net displacement across this type of normal fault-system
425 (synthetic-antithetic pairs) may generate a conspicuous sedimentary basin due to hangingwall collapse.
426 Faulting inception at this site should date back to the Middle Pleistocene, because it controlled the
427 thickening of the continental infill of the basin since the *San Mauro Fm*. deposition.

428 The structural style so far imaged at the Verupola Valley resembles that observed from geomorphology
429 elsewhere along the PSDFS. In particular, the close connection of a SW-dipping master fault with antithetic
430 planes and an evident hangingwall collapse guiding depocenter migration look similar to : i) the fault zones
431 exposed at several paleoseismological trench sites (Figs. 9 and 10d; Cinti *et al.* 2011); ii) the whole PSDFS as
432 revealed by geological evidence and field mapping (Giaccio *et al.* 2012; Pucci *et al.* 2014); iii) the shallow
433 faults revealed by high-resolution *Vp* tomographic images in the Paganica sector (Improta *et al.* 2012); iv)
434 the crustal-scale architecture of normal faults inferred by seismological data of the 2009 seismic sequence
435 (Chiaraluce *et al.* 2011; Valoroso *et al.* 2013, 2014; Section 2.1, Fig. 1c).

436 As a consequence, we conclude that this extensional structural style is scale-independent, because it
437 persists from the outcrop to the basin scale.

438 The tectonic origin of the Verupola Valley with its very shallow upper fault terminations imply that in the
439 San Demetrio sector of the PSDFS the active portion of one of its main fault segments (SGF, Section 2.2) can
440 be confidently mapped farther to the NE than previously reported. This adds a new element in the complex
441 pattern of segmentation of the PSDFS (Fig. 1).

6 Conclusions

The integration and calibration of different geophysical-geological datasets enabled us to explore, with affordable cost of data acquisition and processing time, the tectonic origin of a small valley along the seismogenic fault network (Paganica – San Demetrio fault-system) of the 2009 L'Aquila earthquake region. This valley is a ~30-40 m deep graben (Fig. 10) showing a complex pre-Quaternary basement morphology due to the concurrent activity of three conjugated normal fault splays. These fault splays are a few meters shallow (up to <2m deep) and displace recent sediments. The retrieved structural style is coherent with the regional tectonic setting due to crustal extension.

The approach we used, by avoiding possible over-interpretation and over-simplification due to the use of just one method, is beneficial for future investigations of active faults in complex geological and morphological settings such as those described in this paper.

Acknowledgements

We thank the editor Mark Everett, whose encouragement and suggestions helped us improving the early version of this manuscript. One anonymous reviewer also provided insightful comments. We thank Aldo Iovenitti and Paolo De Matteis for the permission of accessing and drilling/trenching into their properties and for their logistic support. Paola Baccheschi, Carlo Alberto Brunori, Francesca Romana Cinti, Luigi Cucci, Adriano Nardi and Stefania Pinzi provided important contribution during the geophysical surveys and geognostic trenching. Michele Carafa is acknowledged for useful suggestions.

Vp and ERT images were edited with the *Generic Mapping Tools* (Wessel & Smith, 1998); ERT models were computed using the *Tomolab* software (Geoastier, Livorno – Italy, http://www.geoastier.com); surface waves and seismic noise data were analyzed using the *Geopsy* tool (http://www.geopsy.org; Wathelet *et al.* 2004).

465 This work was financially supported by UR5 of Project "*FIRB Abruzzo: High-resolution analyses for assessing*

466 *the seismic hazard and risk of the areas affected by the 6 April 2009 earthquake*", No RBAP10ZC8K_005.

REFERENCES

Ahmad, J., Schmitt, D.R., Rokosh, C.D. & Pawlowicz, J.G., 2009. High-resolution seismic and resistivity profiling of a buried Quaternary subglacial valley: Northern Alberta, Canada, *Geol. Soc. Am. Bull.*, **121**, 1570–1583, doi: 10.1130/B26305.1.

Atzori, S., Hunstad, I., Chini, M., Salvi, S., Tolomei, C., Bignami, C., Stramondo, S., Trasatti, E., Antonioli, A. & Boschi, E., 2009. Finite fault inversion of DInSAR coseismic displacement of the 2009 L'Aquila earthquake (central Italy), *Geophys. Res. Lett.*, **36**, L15305, doi: 10.1029/2009GL039293.

Bard, P.Y., Cadet, H., Endrun, B., Hobiger, M., Renalier, F., Theodulidis, M., Ohrnberger, D., Fäh, F., Sabetta, F. & Teves-Costa, P., 2010. From non-invasive site characterization to site amplification: Recent advances in the use of ambient vibration measurements, *Earthquake Engineering in Europe*, **17**, Part 2, 105–123, doi: 10.1007/978-90-481-9544-2_5.

Bertini, T. & Bosi, C., 1993. La tettonica quaternaria della conca di Fossa (L'Aquila), *Il Quaternario*, **6**, 293–314.

Blakely, R.J. & Simpson, R.W., 1986. Approximating edges of source bodies from magnetic or gravity anomalies, *Geophysics*, **51**, 1494-1498.

Blakely, R.J., Wells, R.E., Yelin, T.S., Madin, I.P. & Beeson, M.H., 1995. Tectonic setting of the Portland–Vancouver area, Oregon and Washington: constraints from low-altitude aeromagnetic data, *Geol. Soc. Am. Bull.,**107*** (7), 1051– 1062.

Boncio, P., Pizzi, A., Brozzetti, F., Pomposo, G., Lavecchia, G., Di Naccio, D. & Ferrarini, F., 2010. Coseismic ground deformation of the 6 April 2009 L'Aquila earthquake (central Italy, Mw6.3), *Geophys. Res. Lett.*, **37**, L06308, doi:10.1029/2010GL042807.

Bonnefoy-Claudet, S., Cécile, C., Pierre-Yves, B., Fabrice, C., Peter, M., Jozef, K. & Fäh, D., 2006. H/V ratio: a tool for site effects evaluation. Results from 1-D noise simulations, *Geophys. J. Int.*, **167**(2), 827-837, doi: 1O.1111/j.1365-246X.2006.03154.x.

491 Bosi, C. & Bertini, T., 1970. Geologia della media valle dell'Aterno, *Mem. Soc. Geol. It.*, **9**, 719 - 777.

492 Bosi, C., Galadini, F., Giaccio, B., Messina, P. & Sposato, A., 2003. Plio-Quaternary continental deposits in the
493 Latium-Abruzzi Apennines: the correlation of geological events across different intermontane basins, *Il*
494 *Quaternario*, **16** (1Bis), 55-76.

495 Bruno, P.P., Castiello, A., Villani, F. & Improta, L., 2013. High-resolution densely spaced wide-aperture
496 seismic profiling as a tool to aid seismic hazard assessment of fault-bounded intramontane basins:
497 application to Vallo di Diano, Southern Italy, *B. Seismol. Soc. Am.*, **103**, 3, 1969-1980, doi:
498 10.1785/0120120071.

499 Burjánek, J., Gassner-Stamm, G., Poggi, V., Moore, J. R. & Fäh, D. 2010. Ambient vibration analysis of an
500 unstable mountain slope, *Geophys. J. Int.*, *180*(2), 820-828.

501 Carafa, M.M.C. & Barba, S., 2011. Determining rheology from deformation data: the case of central Italy,
502 *Tectonics*, **30**, TC2003, doi: 10.1029/2010TC002680.

503 Centamore, E., Crescenti, U., Dramis, F., Bigi, S., Fumanti, F., Rusciadelli, G., Coltorti, M., Chiocchini, M.,
504 Didaskalou, P., Mancinelli, A., Matteucci, R., Micarelli, A., Potetti, M., Pignatti, J.S., Raffi, I., Sirna, G., Conte,
505 G. & Petitta, M., 2006, *Note illustrative della Carta Geologica d'Italia alla scala 1:50.000, Foglio 359*
506 *"L'Aquila"*. APAT – Servizio Geologico d'Italia e Regione Abruzzo – Servizio Difesa del Suolo, S.EL.CA., Firenze.

507 Chiarabba, C., Jovane, L. & Di Stefano, R., 2005. A new view of Italian seismicity using 20 years of
508 instrumental recordings, *Tectonophysics*, **305**, 251-268, doi:10.1016/j.tecto.2004.09.013.

509 Chiarabba, C., Amato, A., Anselmi, M., Baccheschi, P., Bianchi, I., Cattaneo, M., Cecere, G., Chiaraluce, L.,
510 Giaccio, M.G., De Gori, P., De Luca, G., Di Bona, M., Di Stefano, R., Faenza, L., Govoni, A., Improta, L.,
511 Lucente, F.P., Marchetti, A., Margheriti, L., Mele, F., Michelini, A., Monachesi, G., Moretti, M., Pastori, M.,
512 Piana Agostinetti, N., Piccinini, D., Roselli, P., Seccia, D. & Valoroso L., 2009. The 2009 L'Aquila (central Italy)
513 Mw 6.3 earthquake: main shock and aftershocks, *Geophys. Res. Lett.*, **36**, L18308, doi:
514 10.1029/2009GL039627.

515 Chiaraluce, L., Valoroso, L., Piccinini, D., Di Stefano, R. & De Gori, P., 2011. The anatomy of the 2009 L'Aquila
516 normal fault system (central Italy) imaged by high resolution foreshock and aftershock locations, *J. Geophys.*
517 *Res.*, **116,** B12311, doi: 10.1029/2011JB008352.

518 Cinti, F.R., Pantosti, D., De Martini, P.M., Pucci S., Civico R., Pierdominici, S., Cucci, L., Brunori, C.A., Pinzi, S.
519 & Patera, A., 2011. Evidence for surface faulting events along the Paganica fault prior to the 6 April 2009
520 L'Aquila earthquake (central Italy), *J. Geophys. Res.*, **116**, B7, 2156-2202, doi: 10.1029/2010JB007988.

521 Constable, S.C., Parker, R.L. & Constable, C.G., 1987. Occam's inversion: A practical algorithm for generating
522 smooth models from electromagnetic sounding data, *Geophysics*, **52**(3), 289-300.

523 deGroot-Hedlin, C. & Constable, S.C., 1990. Occam's inversion to generate smooth, two dimensional models
524 from magnetotelluric data, *Geophysics*, **55**, 1613-1624.

525 Demanet, D., Renardy, F., Vanneste, K., Jongmans, D., Camelbeeck, T. & Meghraoui, M., 2001. The use of
526 geophysical prospecting for imaging active faults in the Roer Graben, Belgium, *Geophysics*, **66-1**, 78-89, doi:
527 10.1190/1.1444925.

528 Devoti, R., Esposito, A., Pietrantonio, G., Pisani, A.R. & Riguzzi, F., 2011. Evidence of large scale deformation
529 patterns from GPS data in the Italian subduction boundary, *Earth Planet. Sc. Lett.*, **311**, 230-241, doi:
530 10.1016/j.epsl.2011.09.034.

531 Di Giulio, G., Cara, F., Rovelli, A., Lombardo, G. & Rigano R. 2009. Evidences for strong directional resonances
532 in intensely deformed zones of the Pernicana fault, Mount Etna, Italy, *J. Geophys. Res.*, **114**(B10),
533 doi: 10.1029/2009JB006393.

534 Dorn, C., Green, A.G., Jongens, R., Carpentier, S., Kaiser, A.E., Campbell, F., Horstmeyer, H., Campbell, J.,
535 Finnemore, M. & Pettinga, J., 2010. High-resolution seismic images of potentially seismogenic structures
536 beneath the northwest Canterbury Plains, New Zealand, *J. Geophys. Res.*, **115**, B11303, doi:
537 10.1029/2010JB007459.

538 EMERGEO Working Group, 2010. Evidence for surface rupture associated with the Mw 6.3 L'Aquila
539 earthquake sequence of April 2009 (central Italy). *Terra Nova*, **22**(1), 43-51, doi: 10.1111/j.1365-
540 3121.2009.00915.x.

541 Fäh, D., Kind, F. & Giardini, D. 2001. A theoretical investigation of average h/v ratios, *Geophys. J. Int*.
542 145,535 –549.

543 Falcucci, E., Gori, S., Peronace, E., Fubelli, G., Moro, M., Saroli, M., Giaccio, B., Messina, P., Naso, G., Scardia,
544 G., Sposato, A., Voltaggio, M., Galli, P., Galadini, F. & Pantosti, D. 2009. Surface faulting due to the L'Aquila
545 earthquake of April 6th 2009, *Seismol. Res. Lett.*, **80**, 6, doi: 10.1785/gssrl.80.6.940.

546 Galadini, F. & Galli, P., 2000. Active tectonics in the central Apennines (Italy) - input data for seismic hazard
547 assessment, *Nat. Hazards*, **22**, 225–270.

548 Galli, P., Giaccio, B. & Messina, P., 2010. The 2009 central Italy earthquake seen through 0.5 Myr-long
549 tectonic history of the L'Aquila faults system, *Quaternary Sci. Rev.*, **29**, 27-28, 3768-3789, doi:
550 10.1016/j.quascirev.2010.08.018.

551 Galli, P., Giocoli, A., Peronace, E., Piscitelli, S., Quadrio, B. & Bellanova, J., 2013. Integrated near surface
552 geophysics across the Mount Marzano Fault System (southern Italy): seismogenic hints, *Int. J. Earth Sci.*
553 *(Geol. Rundsh.)*, doi: 10.1007/s00531-013-0944-y.

554 Ghisetti, F. & Vezzani L., 1999. Depths and modes of Pliocene-Pleistocene crustal extension of the
555 Apennines (Italy). *Terra Nova*, **11** , 67-72.

556 Giaccio, B., Galli, P., Messina, P., Peronace, E., Scardia, G., Sottili, G., Sposato, A., Chiarini, E., Jicha, B. &
557 Silvestri, S., 2012. Fault and basin depocentre migration over the last 2 Ma in the L'Aquila 2009 earthquake
558 region, central Italian Apennines, *Quaternary Sci. Rev.*, **56**, 69-88, doi: 10.1016/j.quascirev.2012.08.016.

559 Gibson, P.J, Lyle, P. & George, D.M., 1996. Environmental applications of magnetometry profiling, *Environ.*
560 *Geol.*, **27**, 178-183.

561 Giocoli, A., Galli, P., Giaccio, B., Lapenna, V., Messina, P., Peronace, E., Romano, G. & Piscitelli, S. 2011.
562 Electrical Resistivity Tomography across the Paganica-San Demetrio fault system (L'Aquila 2009 earthquake),
563 *B. Geofis. Teor. Appl.*, **52-3**, 457-469, doi: 10.4430/bgta0029.

564 Griffiths, D.H. & Barker, R.D., 1993. Two-dimensional resistivity imaging and modelling in areas of complex
565 geology, *J. Appl. Geophys.*, **29**, 211-226.

566 Gupta, A. & Scholz, C.H., 2000. A model of normal fault interaction based on observations and theory, *J.*
567 *Struct. Geol.*, **22**(7), 865-879, ISSN 0191-8141, http://dx.doi.org/10.1016/S0191-8141(00)00011-0.

568 Hallof, P.G., 1957. *On interpretation of resistivity and induced polarization measurements*. PhD thesis,
569 Massachusetts Institute of Technology.

570 Herrero, A., Improta, L., Zollo, A., Dell'Aversana, P. & Morandi, S., 2000. 2-D nonlinear traveltime
571 tomography by multi-scale search: Imaging an overthrust structure in the southern Apennines, *Eos Trans.*
572 *AGU, Fall Meet. Suppl.*, 81, 418– 910.

573 Improta, L., Zollo, A., Herrero, A., Frattini, R., Virieux, J. & Dell'Aversana, P., 2002. Seismic imaging of
574 complex structures by non-linear traveltime inversion of dense wide-angle data: Application to a thrust belt,
575 *Geophys. J. Int.*, **151**, 264–278, doi: 10.1046/j.1365-246X.2002.01768.x.

576 Improta, L., Ferranti, L., De Martini, P.M., Piscitelli, S., Bruno, P.P., Burrato, P., Civico, R., Giocoli, A., Iorio, M.,
577 D'Addezio, G. & Maschio, L. 2010. Detecting young, slow-slipping active faults by geologic and
578 multidisciplinary high-resolution geophysical investigations: A case study from the Apennine seismic belt,
579 Italy, *J. Geophys. Res.*, **115**, B11307, doi: 10.1029/2010JB000871.

580 Improta, L., Villani, F., Bruno, P.P., Castiello, A., De Rosa, D., Varriale, F., Punzo, M., Brunori, C.A., Civico, R.,
581 Pierdominici, S. & Berlusconi, A. 2012. High-resolution controlled-source seismic tomography across the
582 Middle Aterno basin in the epicentral area of the 2009, Mw 6.3, L'Aquila earthquake (central Apennines,
583 Italy), *Italian Journal of Geosciences*, **131(**3**)**, 373-388, doi: 10.3301/IJG.2011.35.

584 Kvaerna, T., & Ringdahl, F., 1986. Stability of various f-k estimation techniques, Semiannual Technical
585 Summary, *NORSAR Scientific Report*, 29 –40.

586 Loke, M.H. & Barker, R.D., 1995. Least-square inversion of apparent resistivity pseudosections, *Geophysics*,
587 **60**, 1682-1690.

588 Loke, M.H. & Dahlin, T., 2002. A comparison of the Gauss-Newton and quasi-Newton methods in resistivity
589 imaging inversion, *J. Appl. Geophys.*, **49**, 149-162.

590 Mancini, M., Cavuoto, G., Pandolfi, L., Petronio, C., Salari, L. & Sardella, R., 2012. Coupling infill history and
591 mammal biochronology in a Pleistocene intramontane basin: the case of western L'Aquila Basin (central
592 Apennines, Italy), *Quatern. Int.*, **267**, 62-77, http://dx.doi.org/10.1016/j.quaint.2011.03.020.

593 Mc Calpin J. P., (Ed.) 2009. *Paleoseismology*, 2nd edn, Academic, San Diego, California, ISBN: 978-0-12-
594 373576-8.

595 Meghraoui, M., Camelbeeck, T., Vanneste, K., Brondeel, M. & Jongmans, D., 2000. Active faulting and
596 paleoseismology along the Bree fault, lower Rhine graben, Belgium, *J. Geophys. Res.*, **105**(B6), 13,809–
597 13,841, doi: 10.1029/1999JB900236.

598 Meju, M.A., Gallardo, L.A. & Mohamed, A.K., 2003. Evidence for correlation of electrical resistivity and
599 seismic velocity in heterogeneous near-surface materials, *Geophys. Res. Lett.*, **30**(7), 1373,
600 doi:10.1029/2002GL016048.

601 Montone, P., Mariucci, M.T. & Pierdominici, S., 2012. The Italian present-day stress map, *Geophys. J. Int.*,
602 **189**, 705–716, doi: 10.1111/j.1365-246X.2012.05391.x.

603 Morelli, G., & Labrecque D.J., 1996. Advances in ERT inverse modelling, *European Journal of Environmental*
604 *and Engineering Geophysics*, **1**, 171-186.

MS–AQ Working Group, 2010. Microzonazione sismica per la ricostruzione dell'area aquilana. Regione Abruzzo – Dipartimento della Protezione Civile, L'Aquila, 3 vol., available at: http://www.protezionecivile.gov.it/jcms/it/view_pub.wp?contentId=PUB25330.

Nakamura, Y., 1989. A method for dynamic characteristics estimation of subsurface using microtremor on the ground surface. *Q. R. . Rail. Tech.* , **30**, 1, 25-33.

Ohrnberger, M., Schisselé, E., Cornou, C., Bonnefoy-Claudet, S., Wathelet, M., Savvaidis, A., Scherbaum, F. & Jongmans, D., 2004 Frequency wavenumber and spatial autocorrelation methods for dispersion curve determination from ambient vibration recordings, in *Proc. 13th World Conference on Earthquake Engineering*, Vancouver, B.C., Canada, 1–6 August 2004, paper no. 0946.

Patacca, E., Scandone, P., Di Luzio, E., Cavinato, G.P. & Parotto, M. 2008. Structural architecture of the central Apennines: Interpretation of the CROP 11 seismic profile from the Adriatic coast to the orographic divide, *Tectonics*, **27**, doi:10.1029/2005TC001917.

Pischiutta, M., Salvini F., Fletcher, J., Rovelli, A. & Ben-Zion, Y., 2012. Horizontal polarization of ground motion in the Hayward fault zone at Fremont, California: dominant fault-high-angle polarization and fault-induced cracks, *Geophy. J. Int.*, **188**(3), 1255-1272, doi: 10.1111/j.1365-246X.2011.05319.x.

Podvin, P. & Lecomte, I., 1991. Finite difference computation of traveltimes in very contrasted velocity model: a massively parallel approach and its associated tools, *Geophys. J. Int.*, **105,** 271–284, doi: 10.1111/j.1365-246X.1991.tb03461.x.

Pucci, S., Villani, F., Civico, R., Pantosti, D., Del Carlo, P., Smedile, A., De Martini, P.M., Pons-Branchu, E. & Gueli, A., 2014. Quaternary geology map of the Middle Aterno Valley, 2009 L'Aquila earthquake area (Abruzzi Apennines, Italy), *Journal of Maps*, doi: 10.1080/17445647.2014.927128.

Roberts, G.P., Raithatha, B., Sileo, G., Pizzi, A., Pucci, S., Walker, J.F., Wilkinson, M., McCaffrey, K., Phillips, R.J., Michetti, A.M., Guerrieri, L., Blumetti, A.M., Vittori, E., Cowie, P., Sammonds, P., Galli, P., Boncio, P., Bristow, C. & Walters, R., 2010. Shallow subsurface structure of the 2009 April 6 Mw 6.3 L'Aquila earthquake

surface rupture at Paganica, investigated with ground-penetrating radar, *Geophys. J. Int.*, **183**, 774-790, doi: 10.1111/j.1365-246X.2010.04713.x.

Rovida, A., Camassi, R., Gasperini, P. & Stucchi, M., (eds.), 2011. CPTI11, the 2011 version of the Parametric Catalogue of Italian Earthquakes. Milano, Bologna, last release 2011-12-23, http://emidius.mi.ingv.it/CPTI, doi: 10.6092/INGV.IT-CPTI11.

Salvi, S., Cinti, F.R., Colini, L., D'Addezio, G., Doumaz, F. & Pettinelli, E., 2003. Investigation of the active Celano-L'Aquila fault system, Abruzzi (central Apennines, Italy) with combined ground-penetrating radar and paleoseismic trenching, *Geophys. J. Int.*, **155**, 805-818, doi: 10.1111/j.1365-246X.2003.02078.x.

Sheley, D., Crosby, T., Zhou, M., Giacoma, J., Yu, J., He, R. & Schuster, G.T., 2003. 2-D seismic trenching of colluvial wedges and faults, *Tectonophysics*, **368**, 51–69, doi: 10.1016/S0040-1951(03)00150-1.

Shuhab, D.K., Stewart, R.R., Otoum, M. & Chang, L., 2013. A geophysical investigation of the active Hockley Fault System near Houston, Texas, *Geophysics*, **74**(4), B177-B185, doi: 10.1190/GEO2012-0258.1.

Socco, L.V. & Strobbia, C., 2004. Surface-wave method for near-surface characterization: a tutorial, *Near Surface Geophysics*, **2**, 165–185, doi: 10.3997/1873-0604.2004015.

Speranza, F., Nicolosi, I., Ricchetti, N., Etiope, G., Rochette, P., Sagnotti, L., De Ritis, R. & Chiappini, M., 2009. The "Sirente crater field", Italy, revisited, *J. Geophys. Res.*, **114** (B03103), doi: 10.1029/2008JB005759.

Spudich, P., Hellweg, M., & Lee W. H. K., 1996. Directional topographic site response at Tarzana observed in aftershocks of the 1994 Northridge, California, earthquake: implications for mainshock motions. *Bull. seism. Soc. Am.*, ***86***(1B), S193-S208.

Storz, H., Storz, W. & Jacobs, F., 2000. Electrical resistivity tomography to investigate geological structures of the Earth's upper crust, *Geophys. Prospect.*, **48**, 455-471, doi: 10.1046/j.1365-2478.2000.00196.x.

Tokimatsu, K., 1997. Geotechnical site characterization using surface waves. *1st International Conference on Earthquake and Geotechnical Engineering*, **3**, 1333–1368.

652 Valoroso, L., Chiaraluce L., Piccinini D., Di Stefano R., Schaff D. & Waldhauser F., 2013. Radiography of a
653 normal fault system by 64,000 high-precision earthquake locations: The 2009 L'Aquila (central Italy) case
654 study, *J. Geophys. Res.*, **118**, 1156–1176, doi:10.1002/jgrb.50130.

655 Valoroso, L., Chiaraluce, L. & Collettini, C., 2014. Earthquakes and fault zone structure, *Geology*, **42**, 343-
656 346, doi: 10.1130/G35071.1.

657 Vittori, E., Di Manna, P., Blumetti, A.M., Comerci, V., Guerrieri, L., Esposito, E., Michetti, A.M., Porfido,
658 S., Piccardi, L., Roberts, G.P., Berlusconi, A., Livio, F., Sileo, G., Wilkinson, M., McCaffrey, K.J.W., Phillips,&
659 R.J., Cowie, P.A, 2011. Surface Faulting of the 6 April 2009 M-w 6.3 L'Aquila Earthquake in Central Italy. *Bull.*
660 *seismol. Soc. Am.*, **101**(4) 1507-1530, doi: 10.1785/0120100140.

661 Wathelet, M., Jongmans, D. & Ohrnberger, M., 2004. Surface wave inversion using a direct search algorithm
662 and its application to ambient vibration measurements, *Near Surface Geophysics*, **2**, 211-221.

663 Wessel, P. & Smith, W.H.F. 1998. New, improved version of generic mapping tools released, *Eos Trans.*
664 *AGU*, 79(47), 579–579, doi: 10.1029/98EO00426.

665 Wise, D. J., Cassidy, J. & Locke, C.A., 2003. Geophysical imaging of the Quaternary Wairoa North Fault, New
666 Zealand: A case study, *J. Appl. Geophys*, **53**, 1–16, doi: 10.1016/S0926-9851(03)00013-2.

667 Xia, J., Miller, R.D. & Park, C.B., 1999. Estimation of near-surface shear-wave velocity by inversion of
668 Rayleigh waves, *Geophysics*, **64**, 691–700, doi: 10.1190/1.1444578.

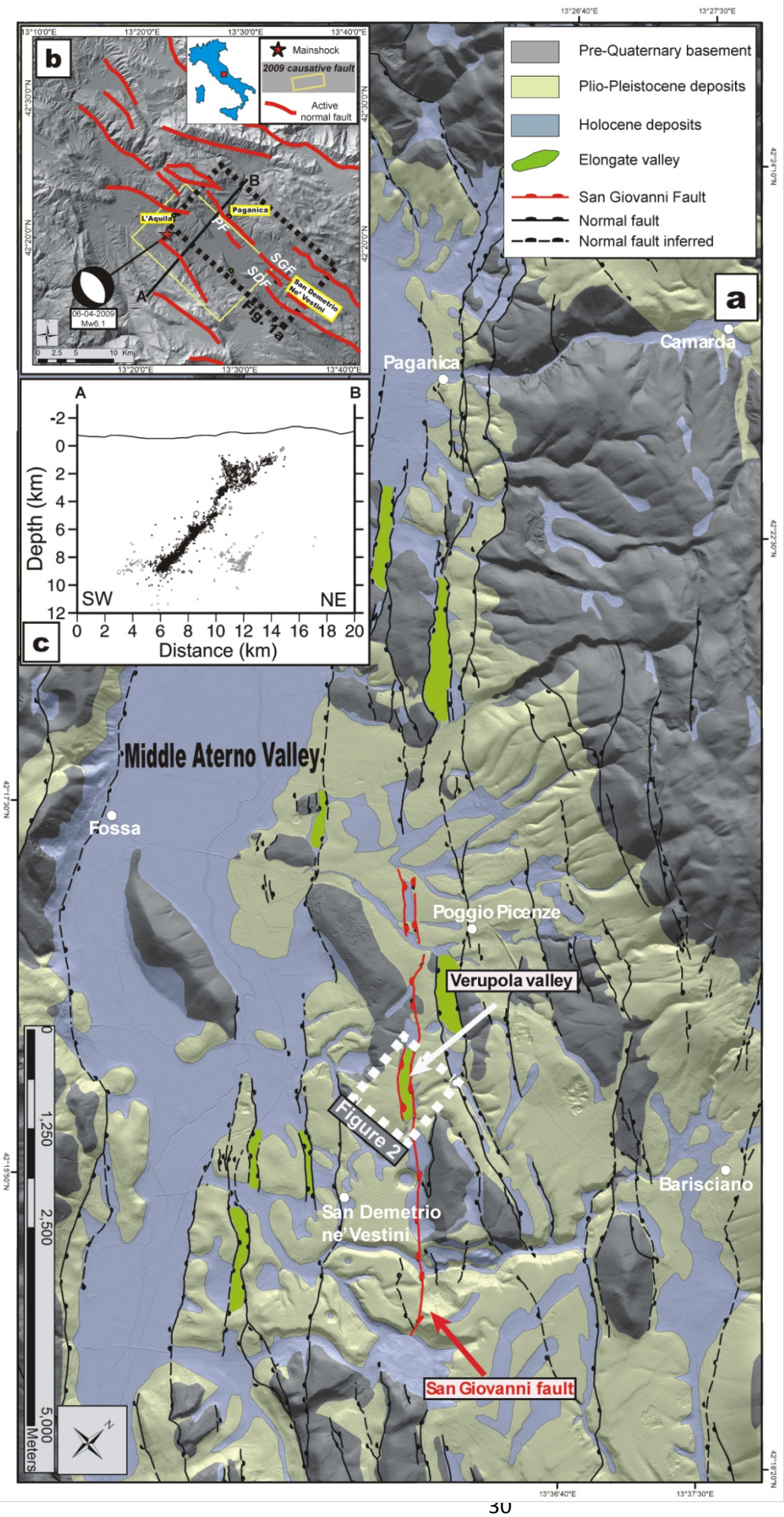

Fig. 1. a) Geological sketch of the Middle Aterno Valley and the Paganica – San Demetrio Fault System (PSDF). The elongate valleys (shown in green) are inferred narrow grabens along the PSDFS, striking at right angles with respect to the regional slope (see Section 2 for details). The white dashed box encloses the small Verupola valley (Fig. 2). *b*) Main Quaternary normal fault systems (in red) in the Abruzzi interior (comprising the PSDFS) and the focal mechanism of the Mw 6.1, 6th April, 2009 mainshock (abbreviations used for the fault systems: PF, Paganica Fault; SDF, San Demetrio Fault; SGF, San Giovanni Fault). *c)* NE-trending cross section of the aftershock distribution (A-B black trace in Fig. 1b - modified after Valoroso *et al.* 2014).

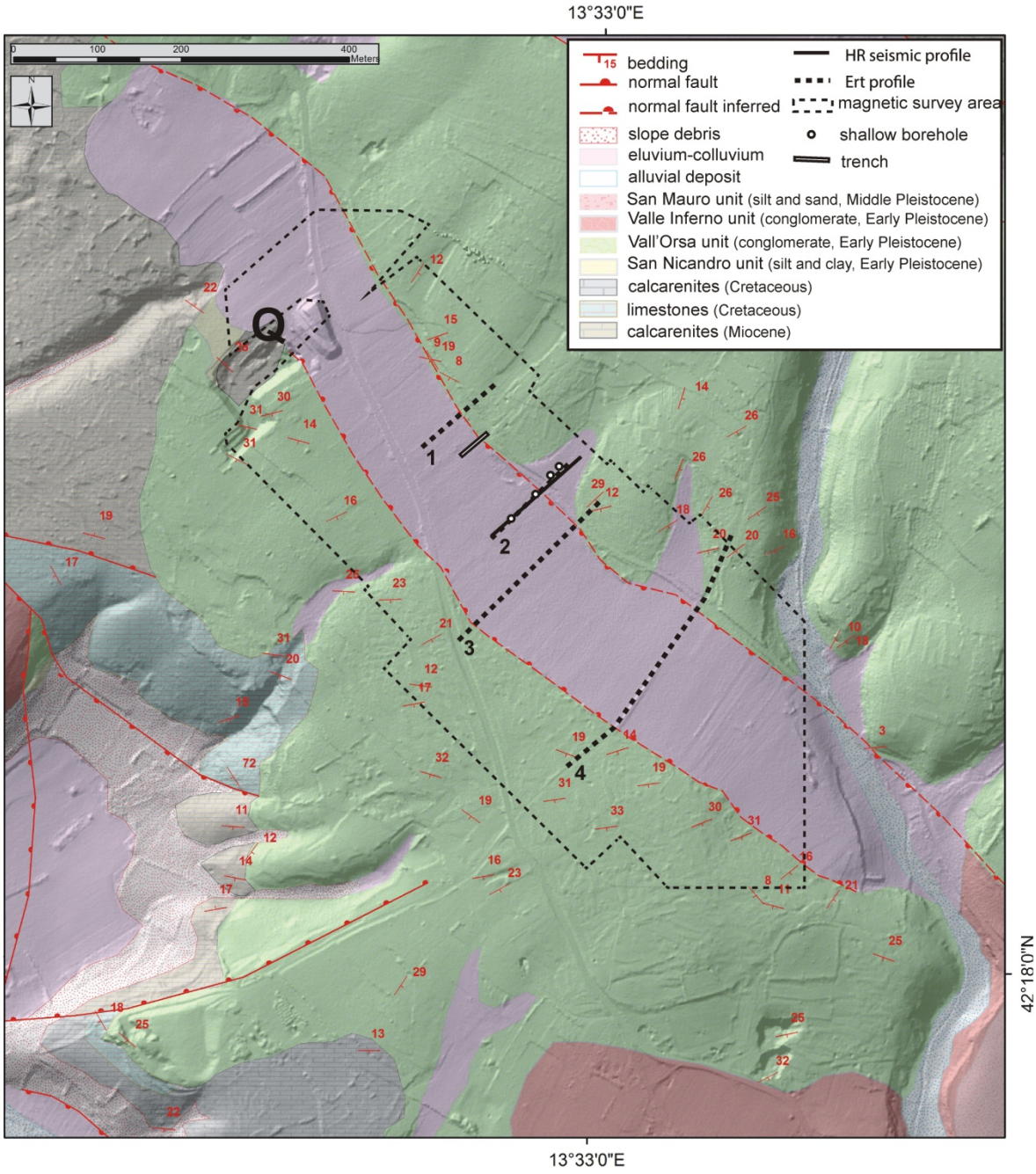

Fig. 2. Geological sketch of the survey site (Verupola Valley) with main morphotectonic features. Location of the HR seismic line, seismic stations, ERT profiles and magnetic survey outline are shown, together with the shallow boreholes and the geognostic trench discussed in the text. ***Q*** indicates the quarry cited in the text.

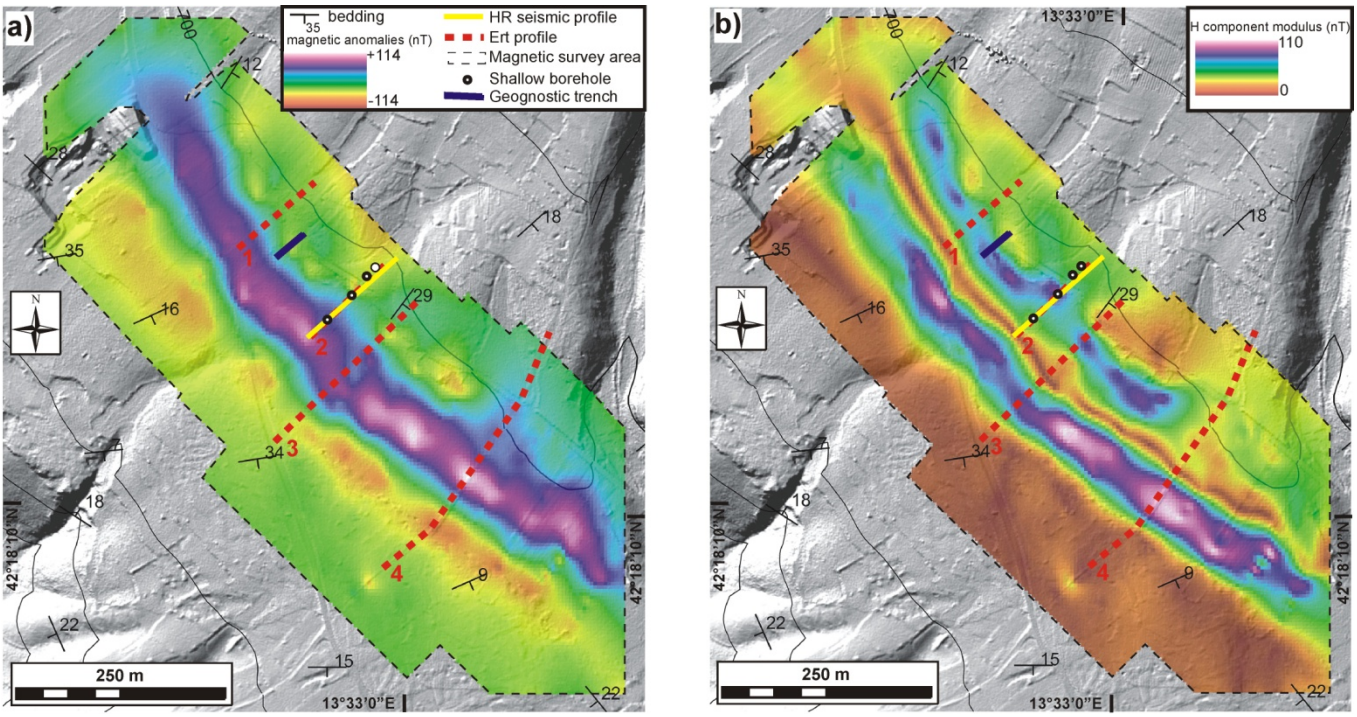

Fig.3: Magnetic data. *a)* map of the gridded anomalies reduced to the magnetic pole; b*)* map of the horizontal components modulus.

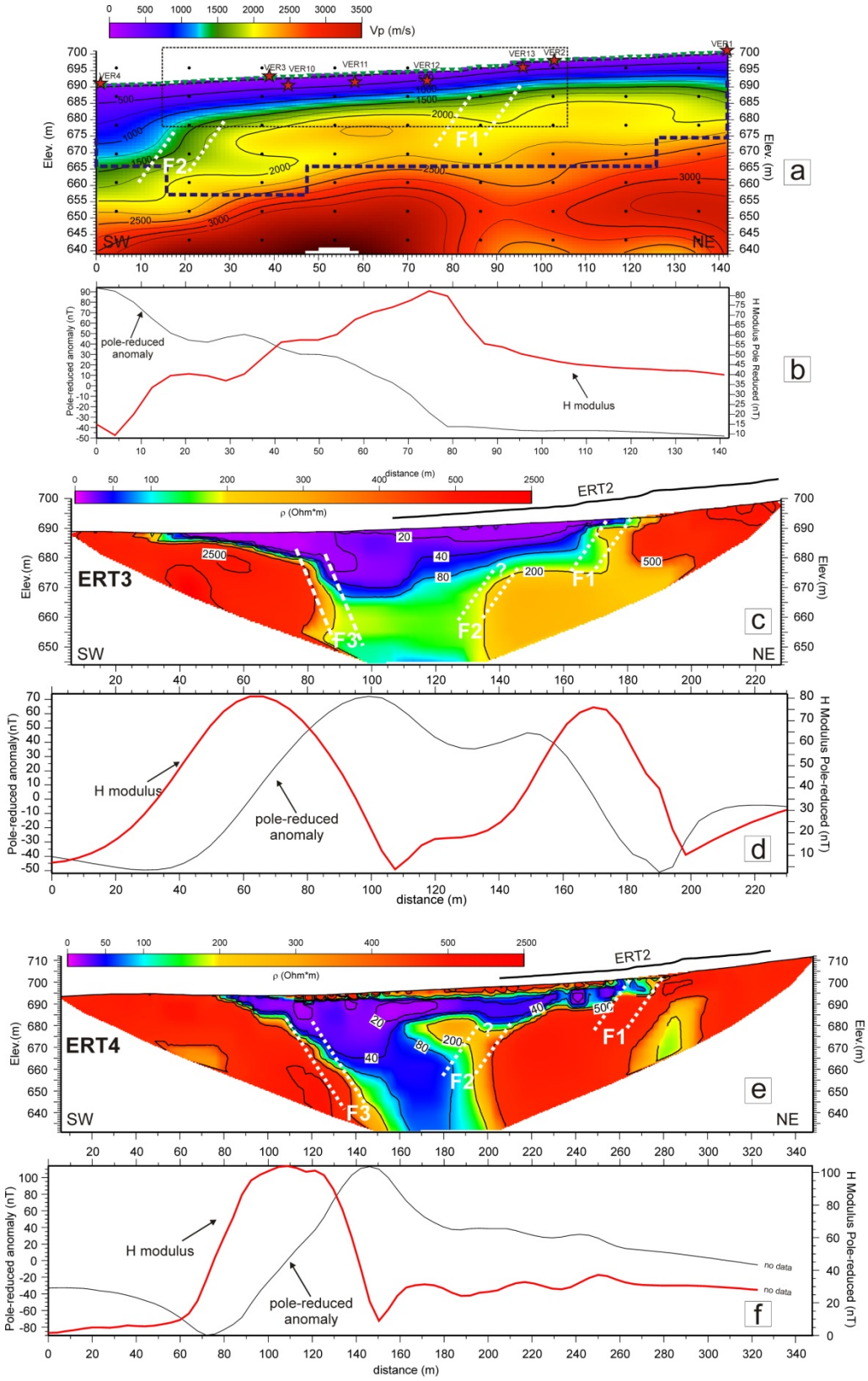

Fig. 4. *a)* Representative HR long-wavelength *Vp* model (black points indicate the 88 parameters; rms = 2.2 s): green triangles are the geophones, blue dashed line indicates resolution depth (assessed by checkerboard test, Fig. S3a), dashed black rectangle indicates the extent of short-wavelength model shown in Fig. 5d, red stars indicate position of seismic stations discussed in Section 4.3, and two possible fault zones inferred from *Vp* lateral changes are shown with dashed white lines (F1 and F2); *b)* 2-D profiles of magnetic anomalies (black line) and horizontal components modulus (red line) along the trace of HR seismic line; *c)* ERT3 model: dashed white lines indicate possible fault splays inferred from lateral resistivity changes (F1, F2 and F3); *d)* 2-D profiles of magnetic anomalies and horizontal components modulus along ERT3 trace; *e)* ERT4 model: dashed white lines as in panel c; *f)* 2-D profiles of magnetic anomalies and horizontal components modulus along ERT4 trace. Note that ERT models are plotted with different scales due to their different sizes.

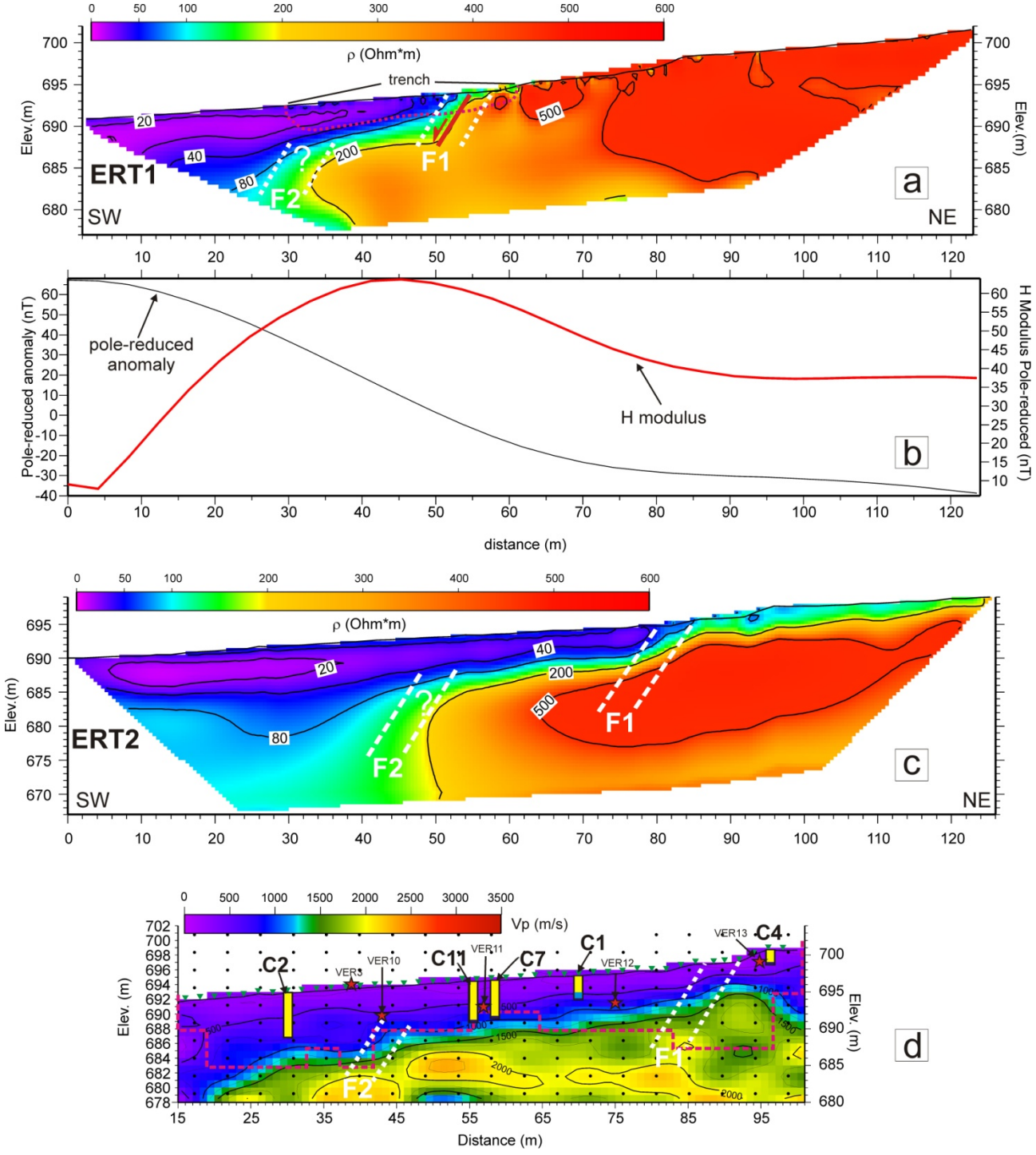

Fig. 5. a) ERT 1 model: white dashed line indicates projected trench perimeter (shown in Fig. 9), red line with arrow indicates normal fault from trench, dashed white lines indicate possible fault splays (F1 and F2) inferred from lateral resistivity changes; b) 2-D profiles of magnetic anomalies and horizontal components modulus along ERT1 trace; c) ERT2 model: dashed white lines as in panel a; d) representative short-wavelength *Vp* model (obtained by cutting the long-wavelength model and using 180 parameters in the final inversion run; rms = 1.7 msec): dashed pink line indicates resolution depth (assessed by checkerboard test; Fig. S3b), black triangles indicate geophones; core locations with simplified stratigraphy are also shown (yellow: clays and sands; pale blue: sands with gravels and caliche; dark blue: weathered conglomerates). ERT2 profile location matches the seismic line (electrode #1, at x=0 m, is coinciding with geophone #1), see Fig. 4a.

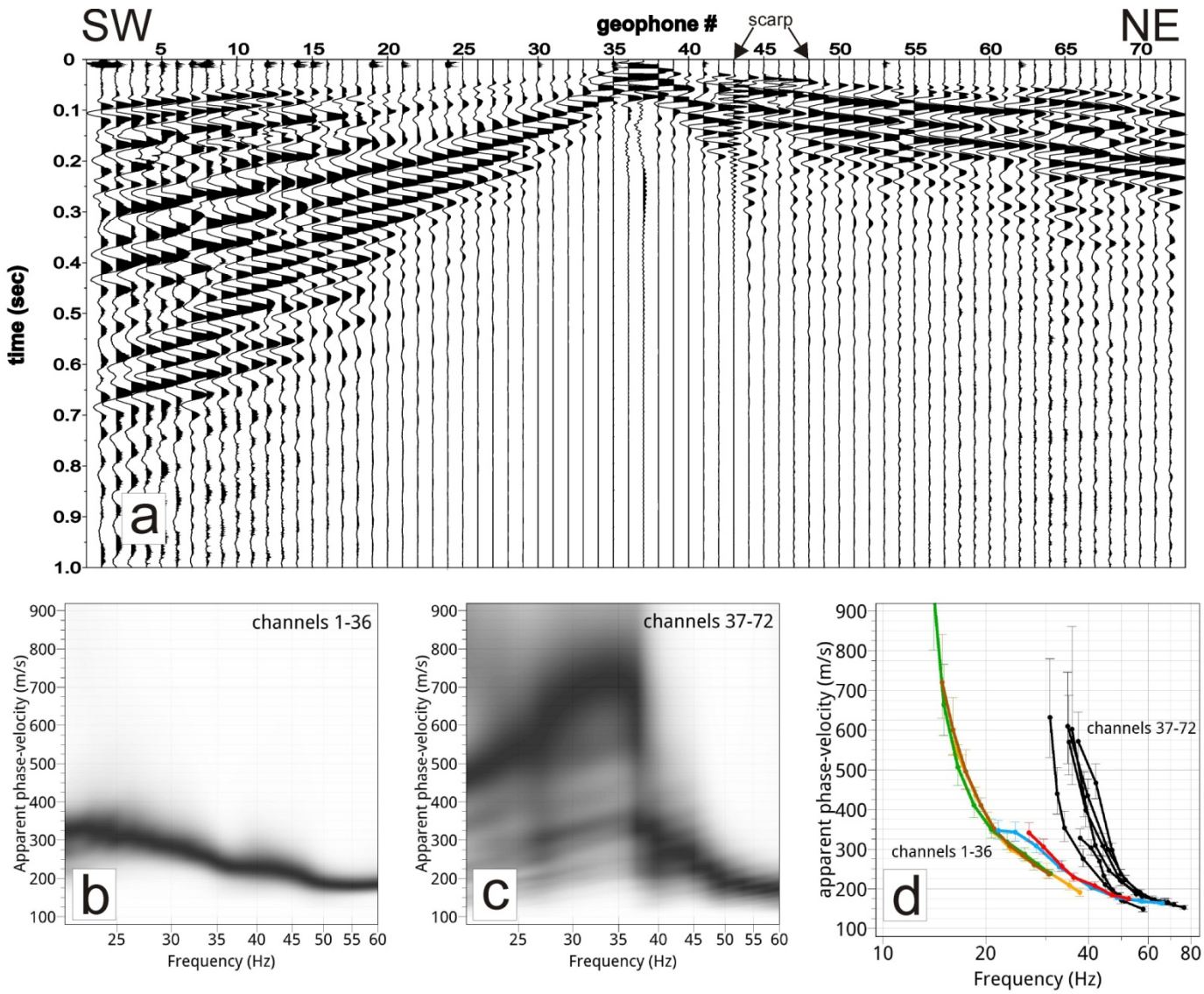

Fig.6. *a)* Seismic traces in the common shot gather used for surface waves analysis (shot position at x=71 m along the seismic line; only trace normalization applied; the base and top of the scarp are indicated by black arrows); *b)* surface-wave dispersion curve using geophones #1-36; *c)* surface-wave dispersion curve using geophones #37-72; *d)* dispersion curves obtained by F-K analysis using traces at different offsets: the coloured curves refer to groups of geophones SW of the scarp; the black curves refer to groups of geophones on the right-part of the array.

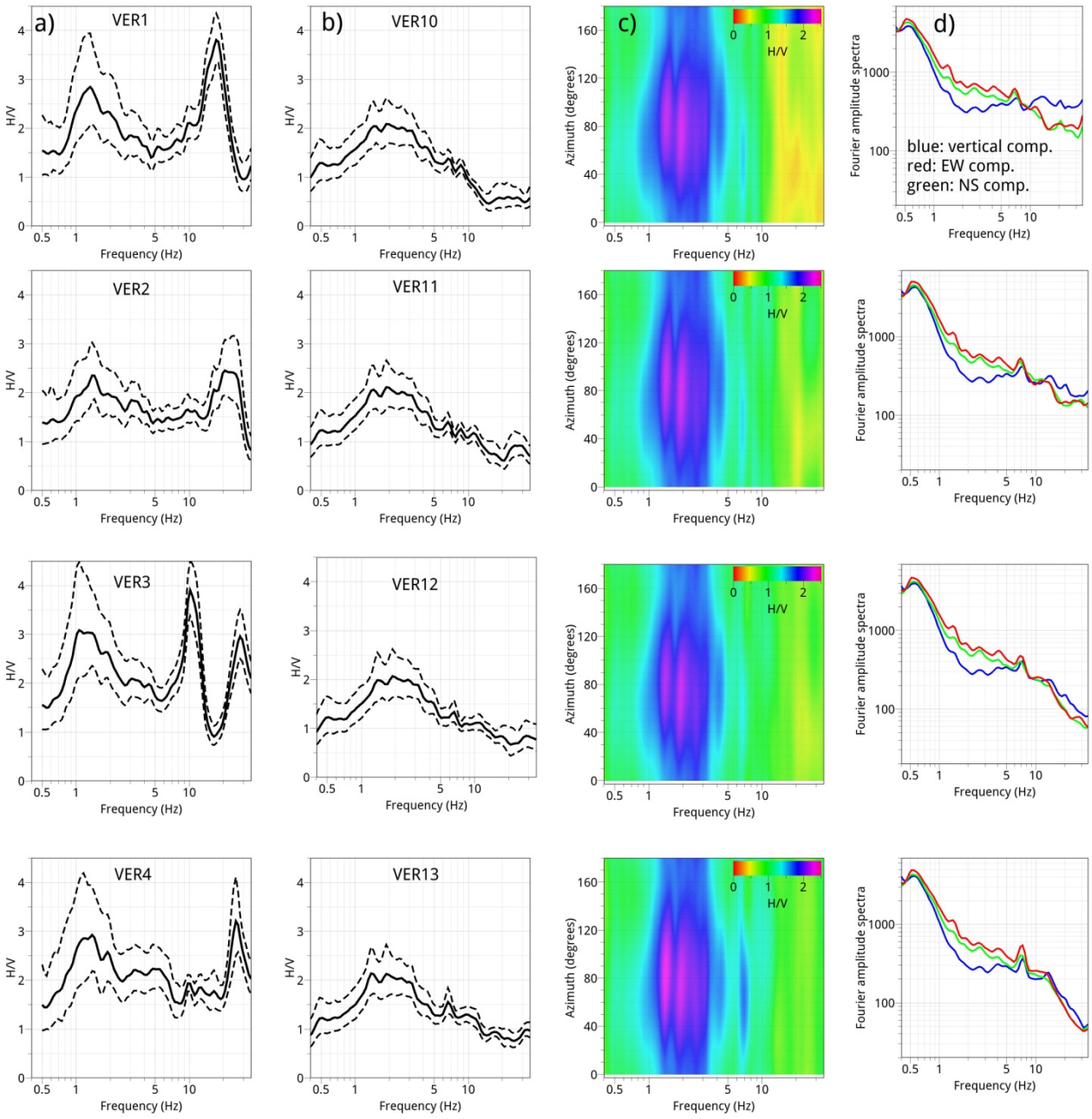

Fig.7. *a)* H/V curves at the ground surface before the execution of the trench (stations VER1, VER2, VER3, VER4); *b)* H/V curves at seismic stations situated inside the trench (station VER10, VER11, VER12, VER13); *c)* directional H/V plots for the sites of panel b; *d)* FAS (on y-axis arbitrary counts) for the measurements of panel *b* (blue curve: vertical component; red curve: EW component; green curve: NS component).

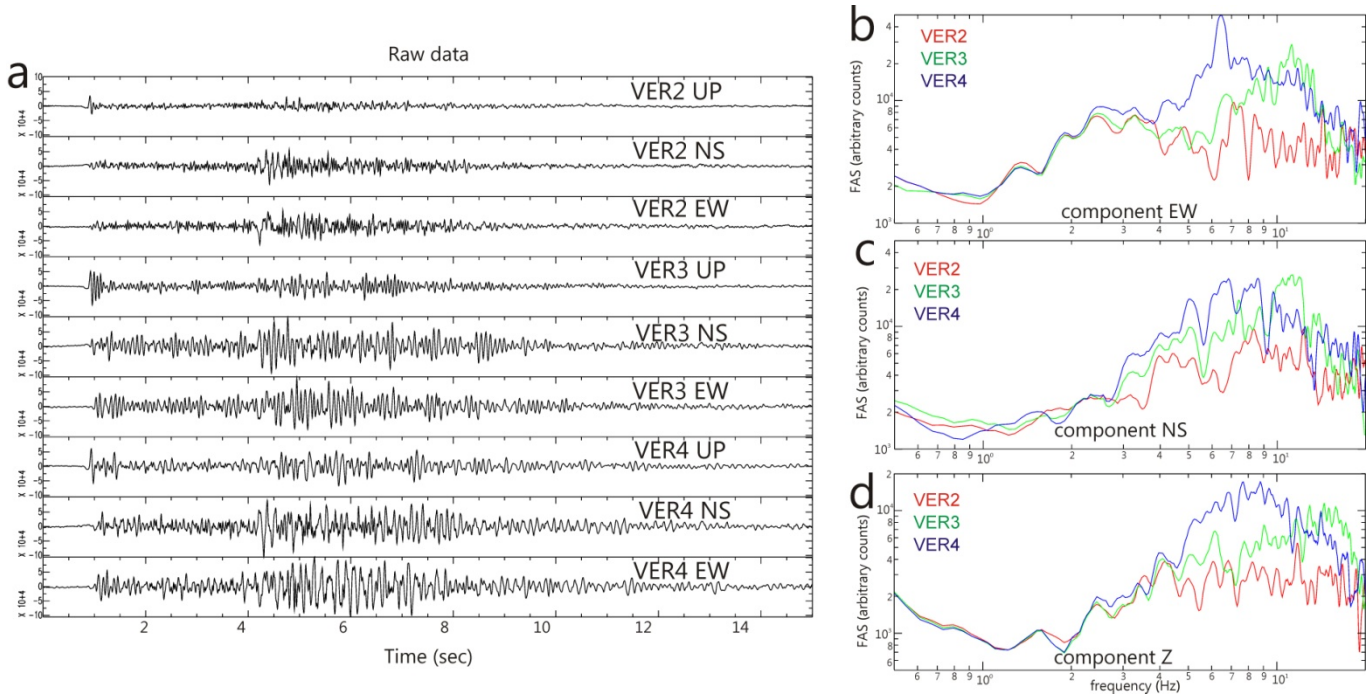

Fig. 8. *a)* Seismograms of the ML 1.7 event recorded by the 3 stations (VER2, VER3, VER4) normalized to the same amplitude scale (arbitrary counts). Fourier amplitude spectra (FAS) of the EW component (*b*), of the NS component (*c*), and of vertical component (*d*).

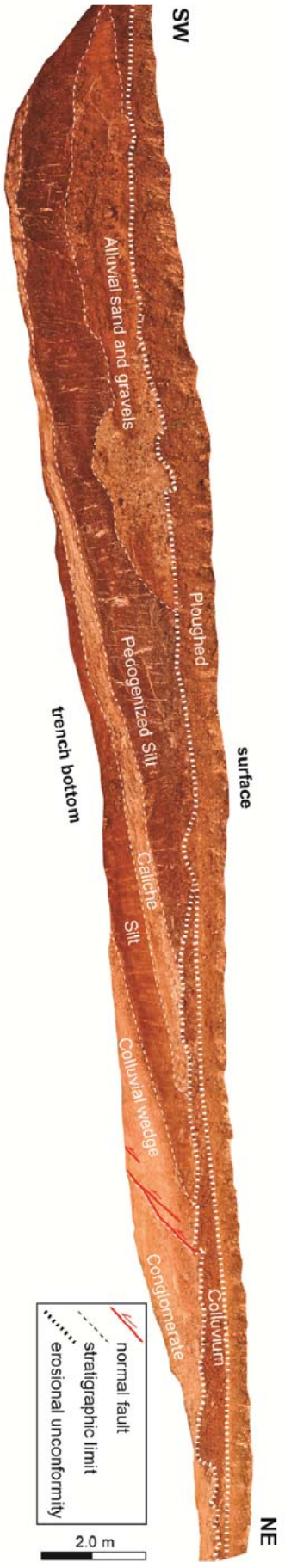

Fig. 9: Simplified log and photomosaic of the geognostic trench showing the fault zone affecting the *Vall'Orsa Fm.* conglomerates and a caliche horizon (possibly Late Pleistocene in age).

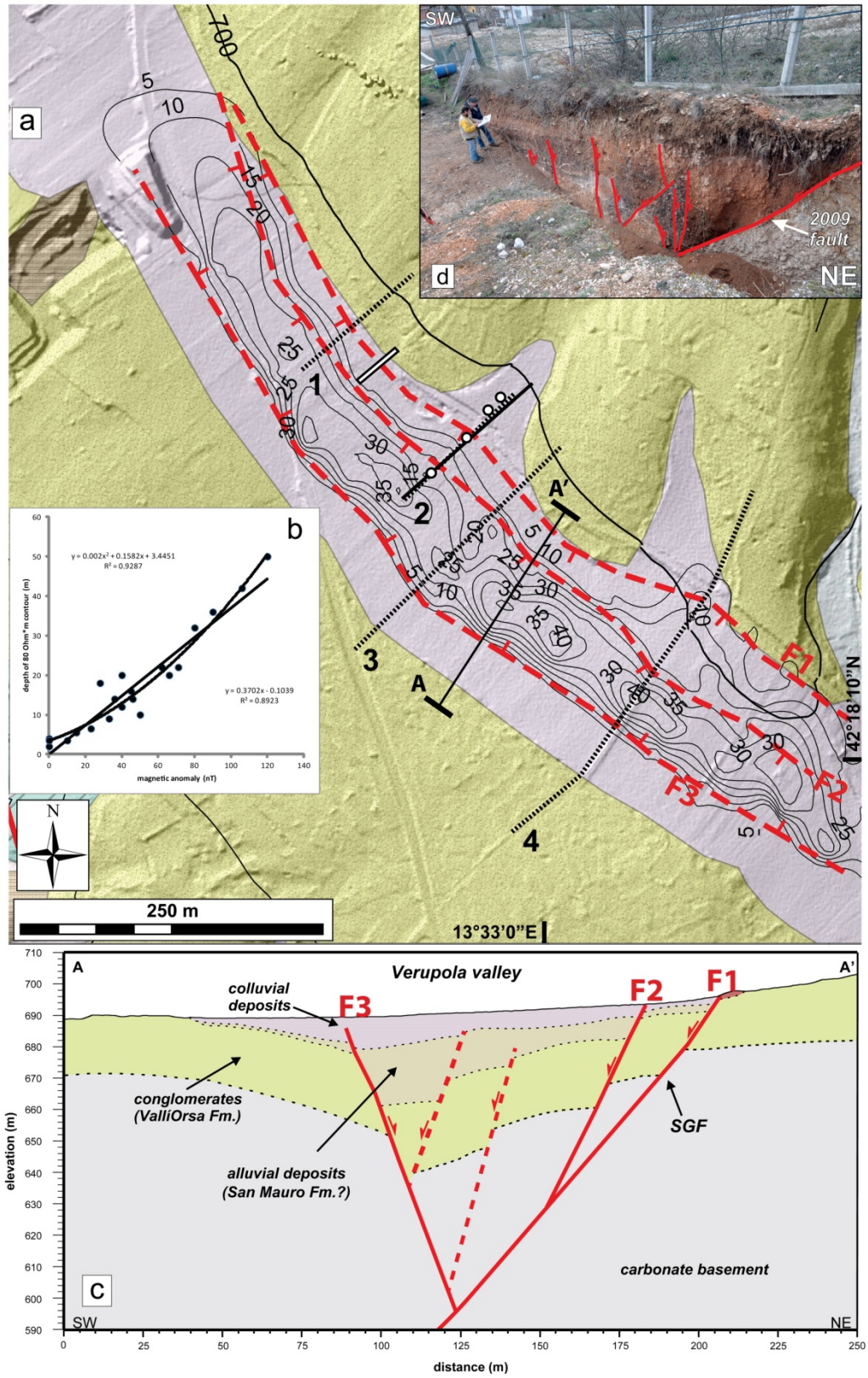

Fig. 10. a) Structural scheme of the Verupola Valley inferred from the integrated geophysical and geological data presented in Sections 4.1, 4.2 and 4.3: dashed red lines indicate normal faults (tick on the downthrown side), whereas thin contour lines indicate the thickness of the sandy-clayey infill (defined as the layer with resistivity ρ<80 Ohm*m) inferred from linear correlation with magnetic intensity (Fig. 10b); b) depth of 80 ohm*m contour (from the four ERT models) vs. magnetic intensity (linear and 2nd order polynomial regression curves are shown; the *p* value of t-Student test is 0.00036, therefore the two datasets are different at a high level of significance); c) Interpretative geological section of the Verupola Valley along trace A-A': the shallow colluvial deposits are clay-rich sediments with low ρ (< 40 Ohm*m) and Vp (< 800 m/s) values; we attribute the underlying sandy and gravelly deposits to the *San Mauro Fm.*, whereas deeper conglomerates belong to the *Vall'Orsa Fm*; the depth and attitude of the top of pre-Quaternary basement are speculative. d) Snapshot of a paleosesimic trench wall across the PSDSF (*Zaccagnini site* of Cinti *et al.* 2011; P.M. De Martini and C.A. Brunori for scale): note that the basic fault pattern at the outcrop scale is very similar to that of the Verupola Valley.

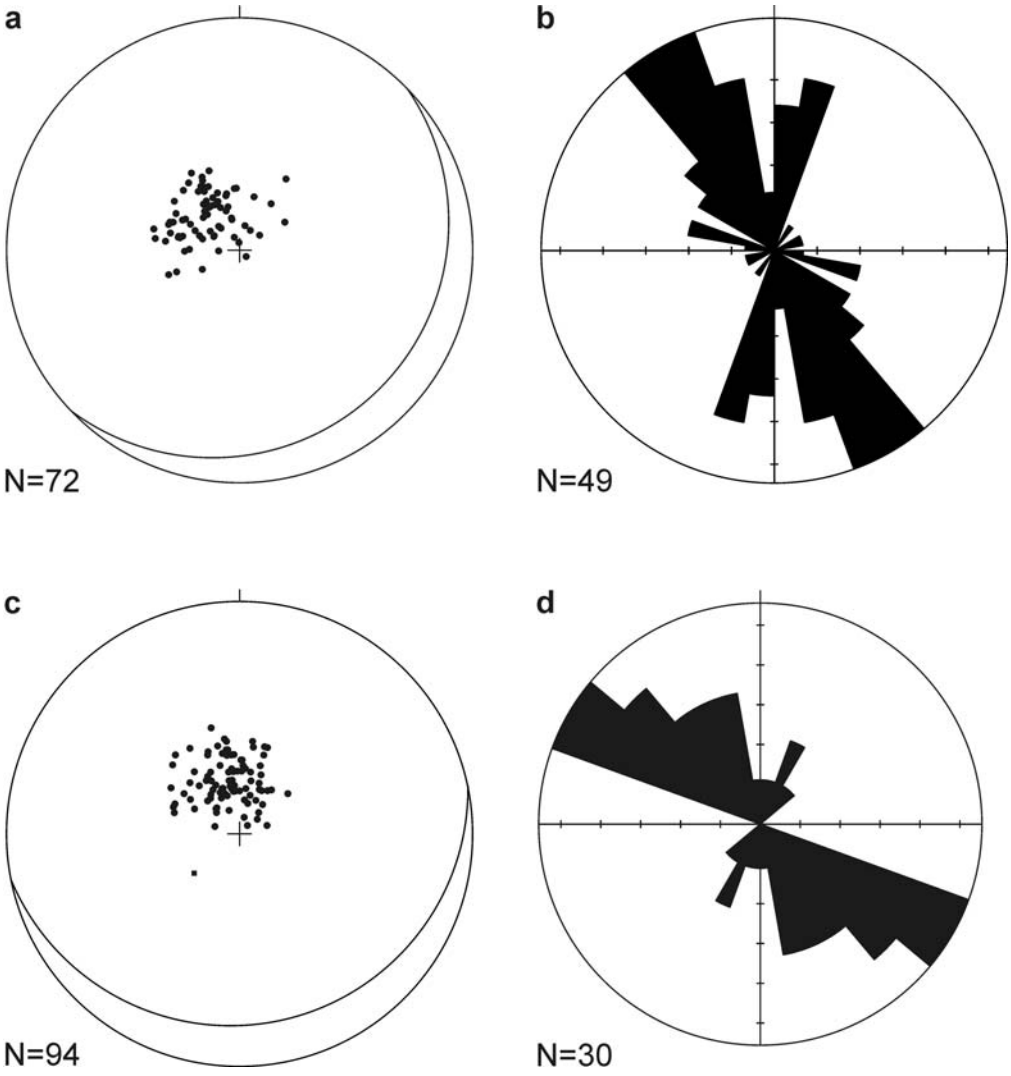

Fig. S1: Meso-structural data from the Verupola site (rock type: Early Pleistocene conglomerates, *Vall'Orsa Fm.*). We measured bedding and joints attitude (dip angle – dip direction notation) over sparse outcrops subdividing collected data into 2 domains: 1) footwall of the SGF; 2) hangingwall of the SGF. *a)* poles to bedding in the SGF footwall (great circle indicates mean plane attitude: 17/136); *b)* rose diagram of joint frequency in the SGF footwall (average strike: N158°); *c)* poles to bedding in the SGF hangingwall (great circle indicates mean plane attitude: 19/168); *d)* rose diagram of joint frequency in the SGF hangingwall (average strike: N145°).

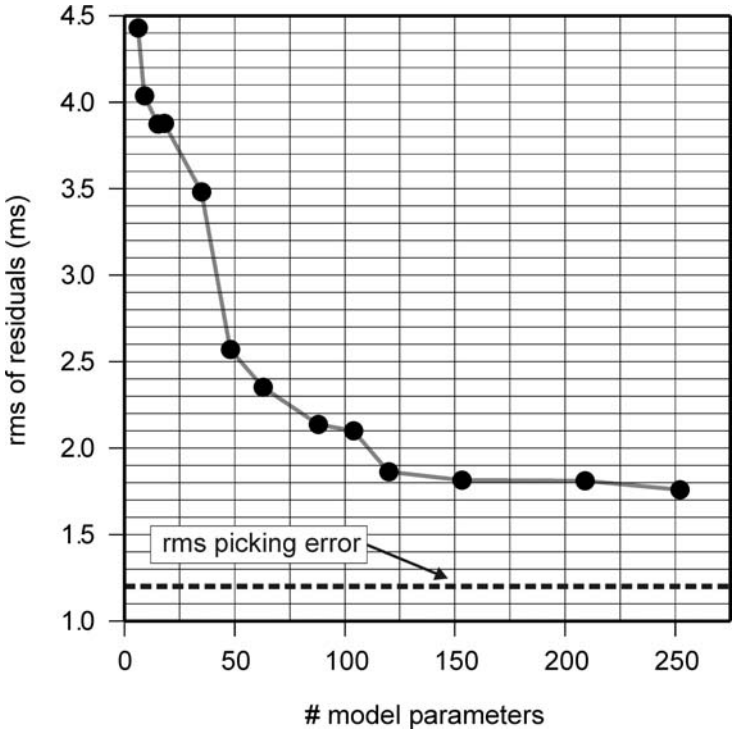

Fig. S2: Multi-scale tomographic inversion of first-arrival traveltimes: decrease of rms residuals (computed – observed traveltimes) with increasing number of model parameters. The dashed black line indicates the rms picking error (~ 1.2 msec).

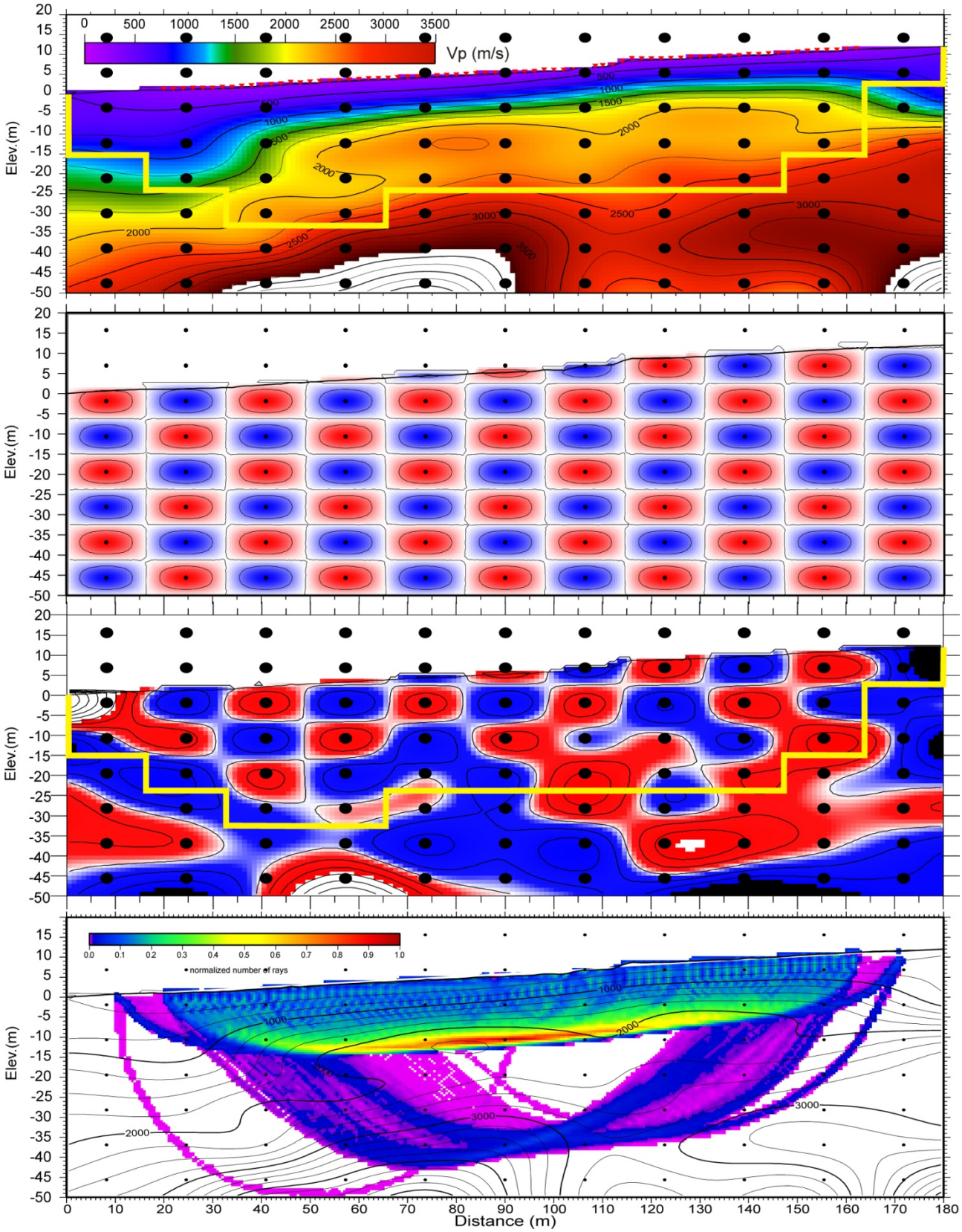

Fig. S3a: From top to bottom: HR long-wavelength *Vp* model shown in Fig. 4a; checkerboard perturbation pattern (*Vp* perturbation range: -50/+50 m/s); checkerboard test result (yellow line indicates inferred resolution depth); normalized rays density inside 1m*1m cells.

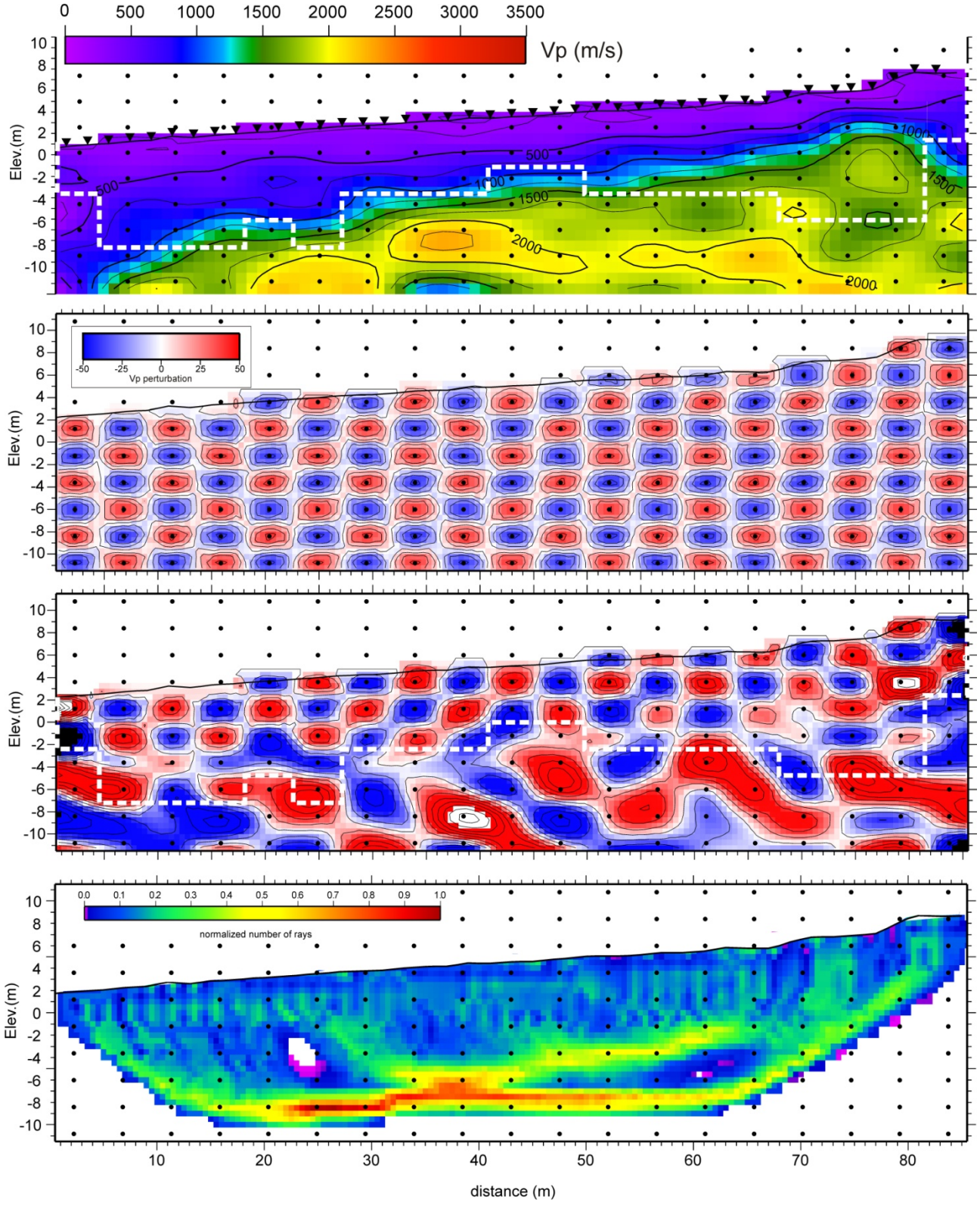

Fig. S3b: From top to bottom: short-wavelength *Vp* model shown in Fig. 5d; checkerboard perturbation pattern (*Vp* perturbation range: -50/+50 m/s); checkerboard test result (dashed white line indicates inferred resolution depth); normalized rays density inside 1m*1m cells.

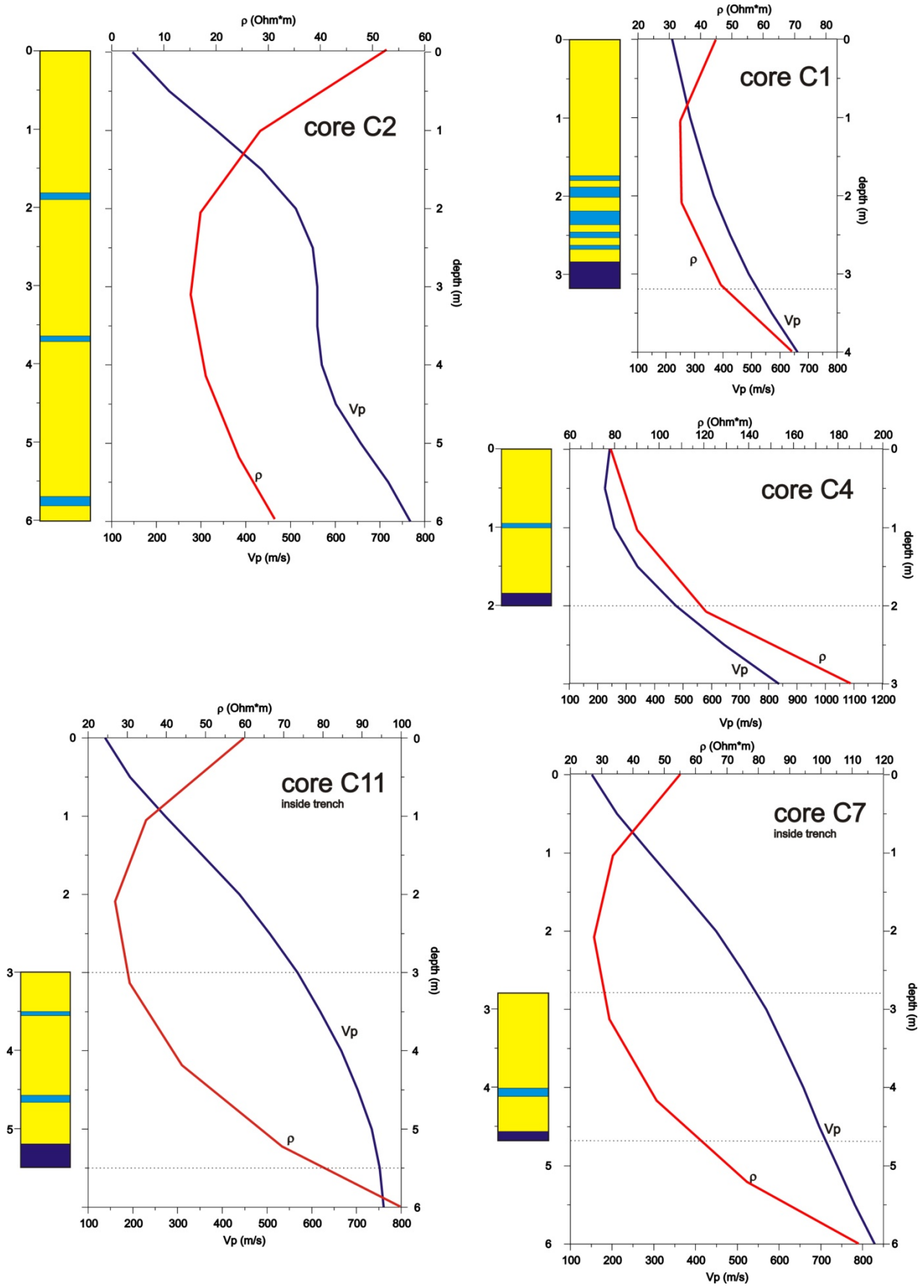

Fig. S4: Detailed stratigraphic logs of 5 shallow boreholes compared with vertical *Vp* and resistivity profiles extracted respectively at each borehole location from the ERT2 profile (Fig. 5c) and the short-wavelength *Vp* model (Fig. 5d). Yellow indicates silts, clays, and fine sands; pale blue indicates calcrete and gravels; dark blue indicates the top weathered portion of Early Pleistocene conglomerates and dense gravels.

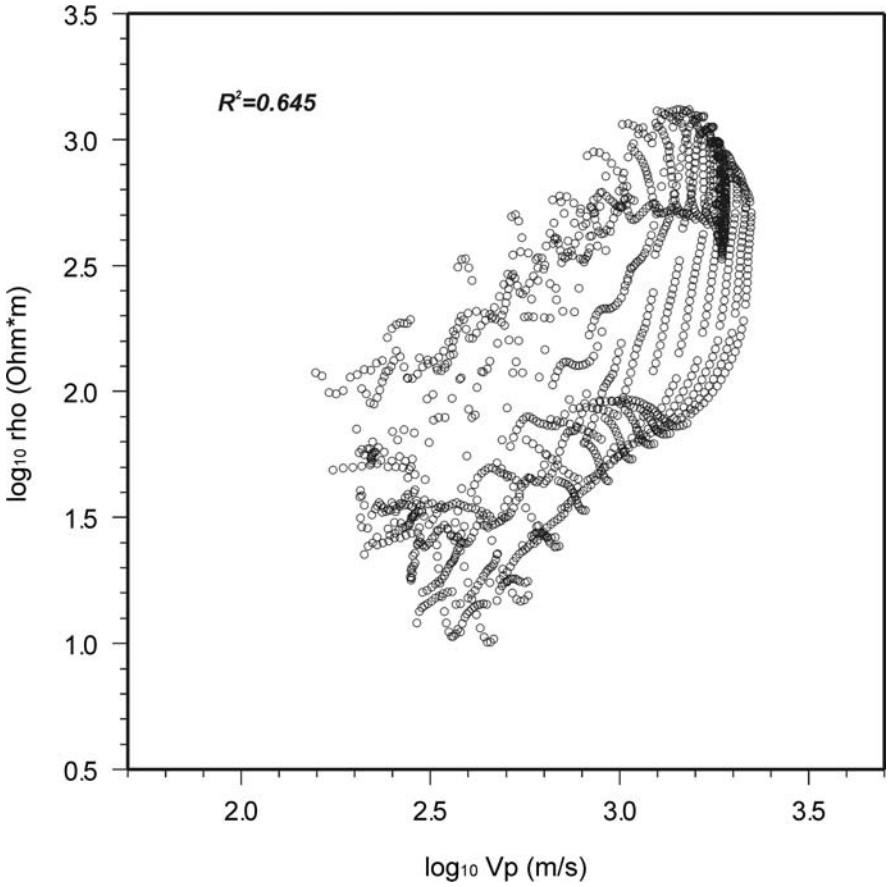

Fig. S5: log-log plot of resistivity values ρ (Ohm*m) from ERT2 model *vs*. corresponding *Vp* values (m/s) from the long-wavelength tomographic model (Pearson correlation coefficient = 0.654).

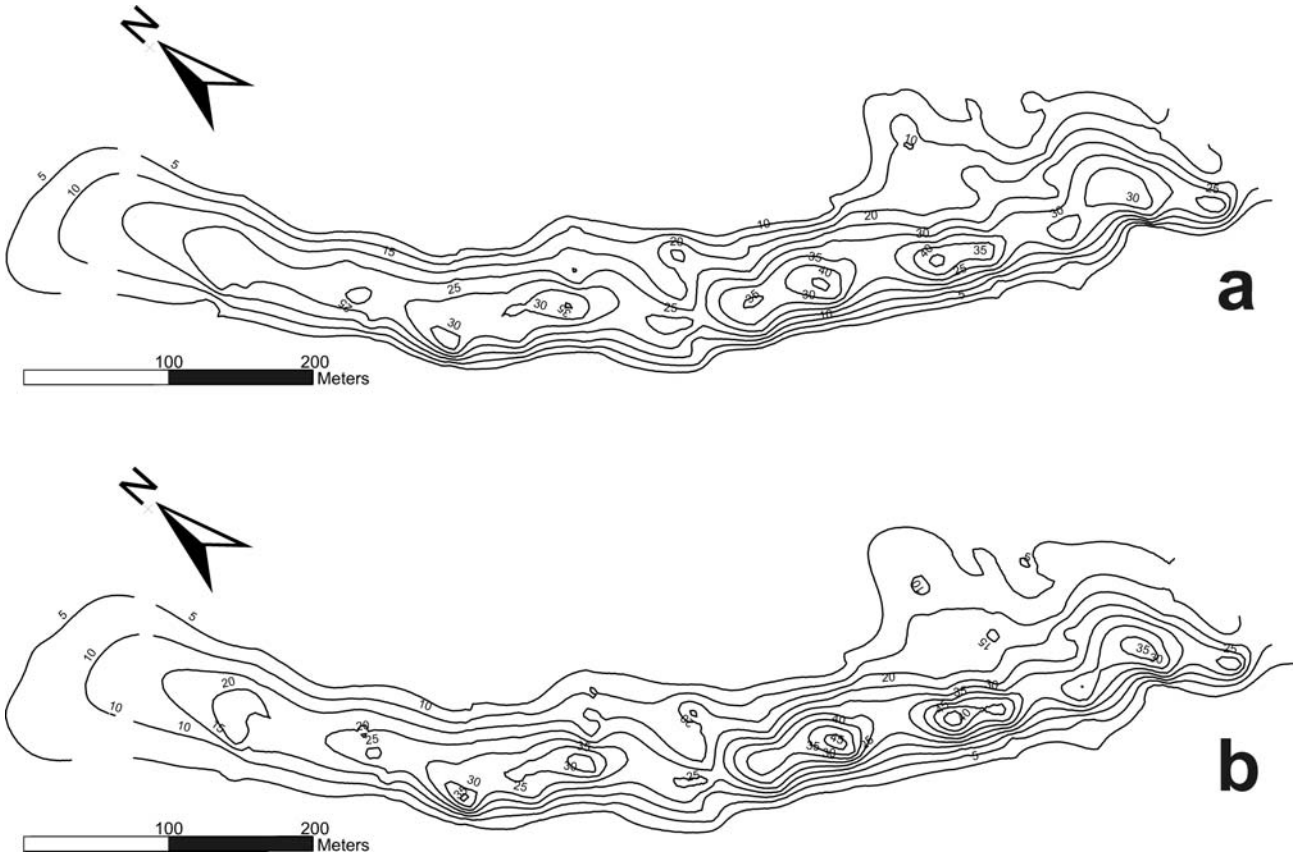

Fig. S6: *a)* contour map of conductive layer thickness obtained using linear regression between the depth of 80 Ohm*m contour and the corresponding magnetic anomaly at the surface (equation shown in Fig. 10b); *b)* same map as panel *a*, obtained using 2nd order polynomial regression between the depth of 80 Ohm*m contour and the corresponding magnetic anomaly at the surface (equation shown in Fig. 10b). The topography of the two maps differs on average by 3.4 m, that is less than 10%.

Table 1: main characteristics of seismic and ERT profiles.

HR seismic profile

(3 Geode© 24-bit seismographs: http://www.geometrics.com)

length (m)	*# geophones*	*# shots*	*geophones eigenfrequency (Hz)*	*receivers spacing (m)*	*energy source*	*average shot spacing (m)*	*# picked traces*	*rms picking (ms)*	*rms residual of final model (ms)*
142	72	75	4.5	2	5 kg sledgehammer	2	5254	1.2	1.5

ERT profiles

(Syscal R2© and Syscal Pro© devices: http://www.iris-instruments.com)

profile name	*length (m)*	*pseudo depth (m)*	*# electrodes*	*electrodes spacing (m)*	*configuration*	*injected current voltage (V)*
ERT1	126	20	64	2	Wenner-Schlumberger	200
ERT2	126	20	64	2	Wenner-Schlumberger	200
ERT3	235	40	48	5	Wenner-Schlumberger + Dipole-Dipole	800
ERT4	355	60	72	5	Wenner-Schlumberger + Dipole-Dipole	800